National Technical University of Athens
Department of Mechanical Engineering

Kneed Walker Design

Model Optimization and CAD Implementation

Kantounias Antonios

September 16, 2023

Abstract

In this report, the kneed bipedal walker is explained. The gait cycle of the model is analyzed and characterized using the return map of the model's gait. In order to do so, the process of generating the Jacobean of the return map is explained. Finally, the model optimization process is reported step by step, and the resulting optimized model is implemented in CAD design.

Contents

1 Introduction

The work presented in this report forms the foundation for the Diploma Thesis, which involves designing and producing a two-dimensional passive walker robot that can be converted to an active one. In previous work conducted by the team, a two-dimensional passive walker was developed using Matlab. This model enables the simulation of a robot's gait based on specific parameters.

The task of designing the robot commences with the determination of optimal design parameters for the model. These parameters are selected based on specific metrics associated with gait stability and robustness. Furthermore, the manufacturability of the robot is a crucial consideration throughout the optimization process.

2 Model Description

The model that has been developed by our team is comprised of four rigid links. Each link has mass and inertia properties. Two of the four links (femoral links) are connected with the hip with a revolute joint (hip joints). The hip joints are free to perform full rotation as the model is not expected to operate near limited angles. Between each of the two remaining links (tibial links) and the corresponding femoral link, a bio-inspired four-bar kinematic linkage intervenes (knee joint). Knee joints, similarly to humans, are kept from hyper-extension by viscoelastic knee cups. The feet curves of the biped are attached to the tibial links and can be of an arbitrary shape. The feet are making contact with a negative slope ground. The gait is performed under the effect of a gravitational acceleration g.

2.1 Generalized Coordinates

The degrees of freedom of the model are six so the model's position in space is described by the generalized coordinates see equation 2.1. The hip's location in space is described by x_H and y_H. Following the femoral link angle related to the transverse from the ground axis is inserted θ_F and ψ_F for the first and the second foot correspondingly. Finally, the femoral related to the tibial link angle is inserted θ_K and ψ_K correspondingly. The generalized coordinates have been marked in Figure 2.1.

$$\mathbf{q} = \left[\begin{array}{c} x_H, y_H, \theta_F, \theta_K, \psi_F, \psi_K \end{array} \right]^\tau \tag{2.1}$$

The model's state is defined by the model's generalized coordinates q and the derivatives of them $\dot{q}$. See equation 2.2

$$\mathbf{x} = \left[\begin{array}{c} \mathbf{q} \\ \dot{\mathbf{q}} \end{array} \right] = \left[\begin{array}{c} x_H, y_H, \theta_F, \theta_K, \psi_F, \psi_K, \dot{x}_H, \dot{y}_H, \dot{\theta}_F, \dot{\theta}_K, \dot{\psi}_F, \dot{\psi}_K \end{array} \right]^\tau \tag{2.2}$$

For the upcoming sections, it is crucial to consider that when foot 1 is in a stance phase, the state variables x_H and y_H can be determined based on the foot's rolling contact condition ($g_{r.c}(\mathbf{q}) = 0$) and the no-penetration condition ($g_{n.p}(\mathbf{q}) = 0$), respectively. Similarly, the state variables $\dot{x_H}$ and $\dot{y_H}$ can be expressed as the derivatives of the foot's rolling contact condition ($\dot{g}_{r.c}(\mathbf{q}, \dot{\mathbf{q}}) = 0$) and the no-penetration condition ($\dot{g}_{n.p}(\mathbf{q}, \dot{\mathbf{q}}) = 0$), as shown in Equation 2.3. This implies that the subspace where foot 1 is in a stance phase can be characterized by the dimensionally reduced state $\hat{\mathbf{x}}$, as presented in Equation 2.4. It's worth noting that the solution to Equation 2.3 is obtained numerically using the differential-algebraic equation solver in Matlab. Specifically the ode15s solver is used.

$$\left[\ x_H, y_H, \dot{x}_H, \dot{y}_H\ \right] = solve(\ g_{r.c}(\mathbf{q}) = 0, g_{n.p}(\mathbf{q}) = 0, \dot{g}_{r.c}(\mathbf{q}, \dot{\mathbf{q}}) = 0, \dot{g}_{n.p}(\mathbf{q}, \dot{\mathbf{q}}) = 0\ ) \tag{2.3}$$

$$\Pi_{SSP_1} : \mathbf{X} \rightarrow \hat{\mathbf{X}}; \mathbf{x} \mapsto \hat{\mathbf{x}} = \left[\ \theta_F, \theta_K, \psi_F, \psi_K, \dot{\theta}_F, \dot{\theta}_K, \dot{\psi}_F, \dot{\psi}_K\ \right]^\tau \tag{2.4}$$

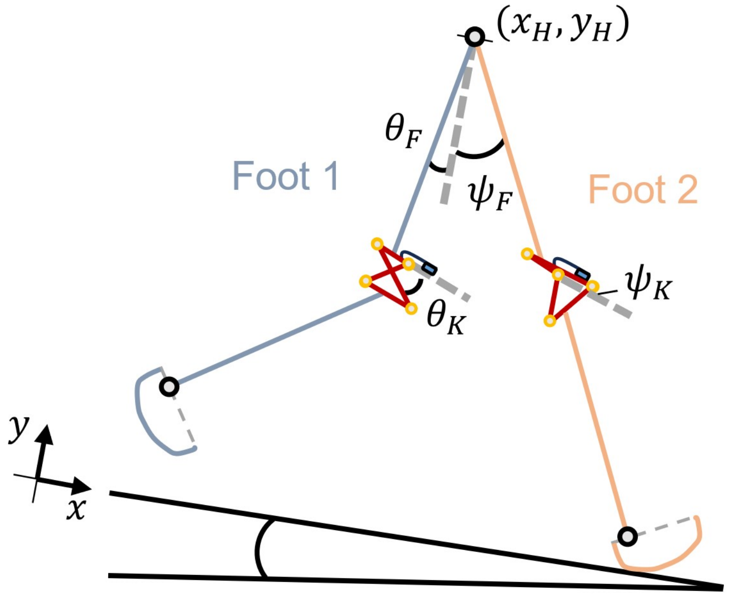

Figure 2.1: The biped model's generalized variables.

2.2 Model Parameters

The biped model's dynamic behavior is related to the parameters of the model. The goal of the model parameterization is to best describe the model's behavior with the minimum number of parameters that have physical meaning in the real world.

The main inertial element of the biped is located at the hip joint and is composed of a body mass M and a moment of inertia I. The femoral links are characterized by their lengths L_F, mass m_F, the center of mass location lF, and link inertia I_F. Similarly, the tibial links are characterized by their lengths L_T, mass m_T, the center of mass location l_T, and link inertia I_T. Additionally, the center of mass of the tibial can be located at a distance l_{Tx} from the tibial axis in the axis-wise transversal direction. See Figure 2.2.

The parameterization of the foot shape and the knee kinematic linkage are out of the scope of this report, so they are not explained here.

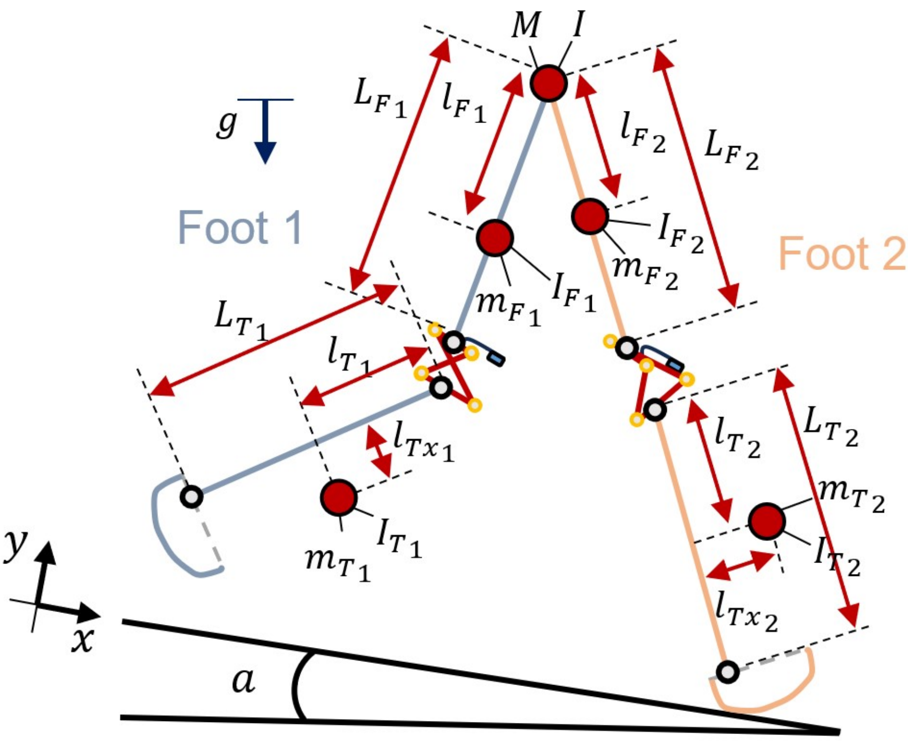

Figure 2.2: The biped's model parameters.

2.3 Model Non-Dimensionalization

In the case of dynamic mechanical systems, it can be seen that the physical dimensions are included in the problem's solution. Non-Dimensionalization is the removal of the physical dimensions from the equations. By non-dimensionalizing a problem, there can be collected metrics that are not related to the physical systems units. A non-dimensional system solution corresponds to solutions for multiple-dimensional systems of different scales but with the same analogies.

In the case of nonlinear dynamic systems, their solution results numerically. The numerical solution of such systems is a computationally expensive procedure. Also, the numerical solver parameters (e.g., discretization, error tolerance) investigation is a demanding procedure that can affect the accuracy and efficiency of the solver. By non-dimensionalizing such nonlinear problems, solutions for multiple scales of the same system are obtained.

From an engineering perspective, it is inferred that the parameter design procedures are more efficient when done in non-dimensional models. In this way the parameters designed once can be applied in multiple physical systems of the same behavior in terms of non-dimensional metrics (e.g. decay rate of a disturbance) but of a different scale. The non-dimensional parameters of the robot are marked in the tables, 2.1, 2.2, 2.3. Finally, the non-dimensionalization of the system reduces the number of the parameters needed to describe the system. See equations, 2.7, 2.8

Parameter Name	Symbol	Definition
Femoral length coef.	L_F^*	$L_F^* = \frac{L_F}{L_{tot}}$
Tibial length coef.	L_T^*	$L_T^* = \frac{L_T}{L_{tot}}$
Femoral CoM coef.	l_F^*	$l_F^* = \frac{l_F}{L_F}$
Tibial CoM coef.	l_T^*	$l_T^* = \frac{l_T}{L_T}$
Tibial CoMx coef.	lx_T^*	$lx_T^* = \frac{lx_T}{L_T}$
Rolling coef.	r^*	$r^* = \frac{r}{L_{tot}}$
Hip mass coef.	M^*	$M^* = \frac{M}{m_{tot}}$
Femoral mass coef.	m_F^*	$m_F^* = \frac{m_F}{m_{tot}}$
Tibial mass coef.	m_T^*	$m_T^* = \frac{m_T}{m_{tot}}$
Hip inertia coef.	I^*	$I^* = \frac{I}{M \cdot L_{tot}^2}$
Femoral inertia coef.	I_F^*	$I_F^* = \frac{I_F}{m_F \cdot L_F^2}$
Tibial inertia coef.	I_T^*	$I_T^* = \frac{I_T}{m_T \cdot L_T^2}$

Table 2.1: Non-Dimensional model basic parameters

Parameter Name	Symbol	Definition
Link 1 length coef.	$l1^*$	$l1^* = \frac{l1}{L_{tot}}$
Link 2 length coef.	$l2^*$	$l2^* = \frac{l2}{L_{tot}}$
Link 3 length coef.	$l3^*$	$l3^* = \frac{l3}{L_{tot}}$
Link 4 length coef.	$l4^*$	$l4^* = \frac{l4}{L_{tot}}$
Link 1 Connection coef.	$l1_c^*$	$l1_c^* = \frac{l1_c}{l1}$
Link 3 Connection coef.	$l3_c^*$	$l3_c^* = \frac{l3_c}{l3}$
Knee cup rotational spring coef.	k_{rot}^*	$k_{rot}^* = \frac{k_{rot}}{m_{tot} \cdot g \cdot L_{tot}}$
Knee cup rotational damper coef.	b_{rot}^*	$b_{rot}^* = \frac{b_{rot}}{m_{tot} \cdot \sqrt{g} \cdot L_{tot}^{1/3}}$

Table 2.2: Non-Dimensional model knee parameters

State Variable Name	Symbol	Definition
Femoral angle coef.	$[\theta, \psi]_F^*$	$[\theta, \psi]_F^* = [\theta, \psi]_F$
Tibial angle coef.	$[\theta, \psi]_K^*$	$[\theta, \psi]_K^* = [\theta, \psi]_K$
Femoral rotational velocity coef.	$\left[\dot{\theta}, \dot{\psi}\right]_F^*$	$\left[\dot{\theta}, \dot{\psi}\right]_F^* = \frac{[\dot{\theta},\dot{\psi}]_F}{\sqrt{g/L_{tot}}}$
Tibial rotational velocity coef.	$\left[\dot{\theta}, \dot{\psi}\right]_K^*$	$\left[\dot{\theta}, \dot{\psi}\right]_K^* = \frac{[\dot{\theta},\dot{\psi}]_K}{\sqrt{g/L_{tot}}}$

Table 2.3: Non-Dimensional state variables

$$m_{tot} = M + 2 \cdot m_F + 2 \cdot m_T \tag{2.5}$$

$$L_{tot} = L_F + L_T \tag{2.6}$$

$$\begin{aligned}
M^* &= \frac{M}{m_{tot}} \overset{eq:2.5}{\Longrightarrow} \\
M^* &= \frac{M_{tot} - 2 \cdot m_F - 2 \cdot m_T}{M_{tot}} \Longrightarrow \\
M^* &= 1 - 2 \cdot m_F^* - 2 \cdot m_T^*
\end{aligned} \tag{2.7}$$

$$\begin{aligned}
L_T^* &= \frac{L_T}{L_{tot}} \overset{eq:2.6}{\Longrightarrow} \\
L_T^* &= \frac{L_{tot} - L_F}{L_{tot}} \Longrightarrow \\
L_T^* &= 1 - L_F^*
\end{aligned} \tag{2.8}$$

3 Model's Gait Cycle

In this section, the biped's model gait cycle is analyzed. In the beginning, the gait's return map is defined. Then, the Jacobian of the return map is calculated with the model's state dimensional reduction. Finally, a Newton-Raphson algorithm is used to determine the fixed points of the return map.

3.1 Introduction to Poincare Map

It is known but not analyzed in this report, that one efficient way to analyze the orbital stability of a continuous dynamic system with periodic orbit, is the Poincare Method. Lets consider the

$n - dimensional$ continuous dynamical system, $\dot{\mathbf{x}} = f(\mathbf{x})$ with $\mathbf{x}\epsilon\mathbf{X}$. Then let's define a $(n-1)-dimensional$ hyperplane of the system's state space $\mathbf{\Sigma} = \{\mathbf{x}\epsilon\mathbf{X}|Condition\}$. It is required that all trajectories of the system starting from $\mathbf{\Sigma}$ flow through $\mathbf{\Sigma}$ (transversality condition). Poincare Map is the discrete dynamical system that maps the continuous dynamical system from its k^{th} crossing of $\mathbf{\Sigma}$ to its $(k+1)^{th}$ crossing of $\mathbf{\Sigma}$. The hyperplane $\mathbf{\Sigma}$ is called the Poincare Section.

Assuming a system that begins from the Poincare Section always returns to it, then the orbital stability analysis problem of the continuous dynamical system is reduced to the stability analysis of a fixed point of the discrete Poincare Map. See Figure 3.1

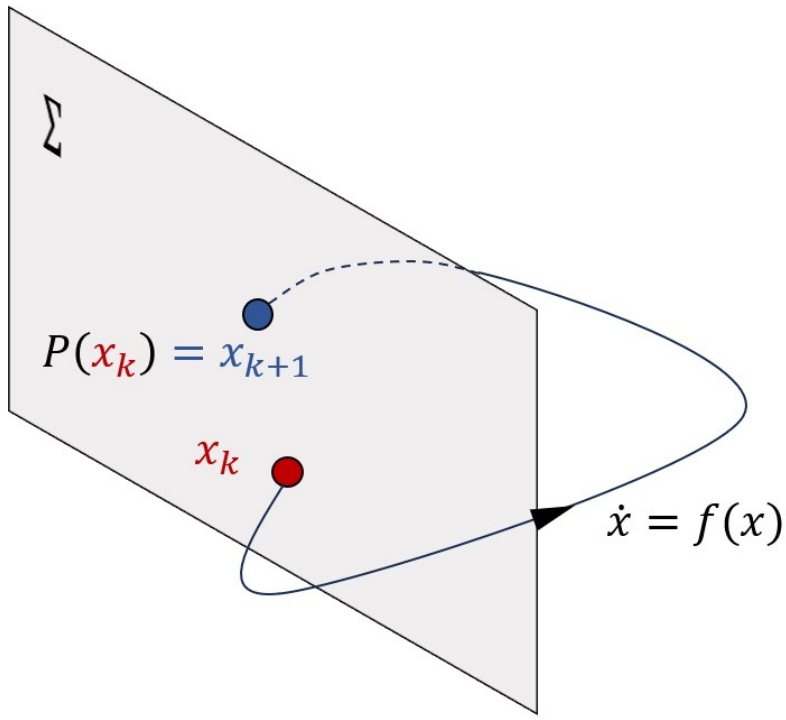

Figure 3.1: Poincare section and Poincare map visualization for a continuous dynamic system with periodic orbit

3.2 Apex Height Poincare Section

To define the biped's Poincare Section, it is essential to establish the phases that the biped goes through during a gait cycle. The first phase, denoted as SSP_1 (single stance phase 1), corresponds to the robot state in which foot 1 is in the stance position while foot 2 is in flight. Similarly, the state in which foot 2 is in the stance position while foot 1 is in flight is defined as SSP_2 (single stance phase 2). Finally, the phase in which both biped feet are in the stance position is known as DSP (double stance phase). These phases of the model are depicted in Figure 3.2.

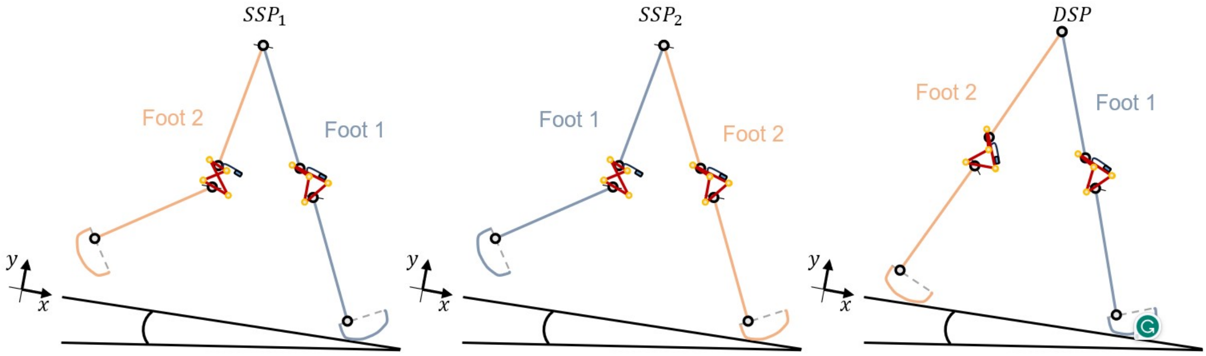

Figure 3.2: The phases in which the model can be. Single Stance Phase 1 (SSP_1), Single Stance Phase 2 (SSP_2) and Double Stance Phase (DSP)

For the generalized model where foot 1 and foot 2 are not identical, to study the gait cycle, the sequence of events needed are presented in the following sequence 3.1

$$SSP_1 \rightarrow DSP \rightarrow SSP_2 \rightarrow DSP \tag{3.1}$$

In the case where foot 1 and foot 2 are identical, the same gait can be produced by interchanging the state values related to foot 1 with those of foot 2. See the sequence 3.2

$$SSP_1 \rightarrow DSP \rightarrow (\theta \leftrightarrows \psi) \rightarrow SSP_1 \rightarrow DSP \rightarrow (\theta \leftrightarrows \psi) \tag{3.2}$$

The apex height at the single stance phase is a well-defined hyperplane of the state space $\hat{\mathbf{x}}$ see equation 2.4. Using the above hyperplane the AH Poincare Section is defined, see equation 3.3. This Poincare section will be used for the rest of the analysis.

$$\mathbf{\Sigma} = \{\hat{\mathbf{x}} \epsilon \hat{\mathbf{X}} | \dot{y}_H = 0\}. \tag{3.3}$$

When projecting the state $\hat{\mathbf{x}}$ to the hyperplane Σ, the state variable θ_F can be expressed using the apex height condition see equation 3.4. In this way, a further state dimensional reduction can be executed see equation3.5. Note that the solution of the equation is done numerically using Newton Raphson method.

$$\theta_F = solve(\dot{y}_H(\hat{\mathbf{x}}) = 0) \tag{3.4}$$

$$\Pi_{\dot{y}_H=0} : \hat{\mathbf{X}} \rightarrow \hat{\hat{\mathbf{X}}}; \hat{\mathbf{x}} \mapsto \hat{\hat{\mathbf{x}}} = \begin{bmatrix} \theta_K, \psi_F, \psi_K, \dot{\theta}_F, \dot{\theta}_K, \dot{\psi}_F, \dot{\psi}_K \end{bmatrix}^T \tag{3.5}$$

In conclusion, the Poincare map of the apex height is presented in equation 3.6

$$\hat{\hat{\mathbf{x}}}_{\mathbf{k+1}} = P_{AH}(\hat{\hat{\mathbf{x}}}_{\mathbf{k}}) \tag{3.6}$$

3.3 Jacobian of the AH Poincare Map

The Jacobian of the Poincare Map is a useful tool to calculate the fixed point of the Poincare Map. Also, the Jacobian of the Poincare Map helps us to linearize the Poincare Map around its fixed point and characterize its local stability. Local stability of the Poincare Map around a fixed point composes the main metric to estimate the general stability of the Poincare map. As mentioned in section 1 stability will be one of the main metrics of the model optimization process. The Jacobian matrix of the Poincare section for the section state $\hat{\hat{x}}_a$ is defined in the bellow equation 3.7.

$$\nabla P_{AH}|_{\hat{\hat{x}}=\hat{\hat{x}}_a} = \frac{\partial P_{AH}}{\partial \hat{\hat{\mathbf{x}}}}|_{\hat{\hat{x}}=\hat{\hat{x}}_a} = \begin{bmatrix} \frac{\partial P_{AH}}{\partial \theta_K} & \frac{\partial P_{AH}}{\partial \psi_F} & \frac{\partial P_{AH}}{\partial \psi_K} & \frac{\partial P_{AH}}{\partial \dot{\theta}_F} & \frac{\partial P_{AH}}{\partial \dot{\theta}_K} & \frac{\partial P_{AH}}{\partial \dot{\psi}_F} & \frac{\partial P_{AH}}{\partial \dot{\psi}_K} \end{bmatrix}_{\hat{\hat{x}}=\hat{\hat{x}}_a} \tag{3.7}$$

The partial derivatives of the AH Poincare Map P_{AH} with respect to a specific state variable (without loss of generality let's say θ_K) are calculated numerically using central differences and a perturbation ε by the bellow expression see equation 3.8. It is acknowledged that perturbing a state variable can influence the overall energy level of the system. However, it is important to note that the system's energy is not constant; it decreases during knee and foot strikes, and the lost kinetic energy is regained through dynamic energy acquired during the robot's descent. In essence, the states of the system are not interlinked by the energy conservation equation. Therefore, while perturbing a state variable may alter the system's energy, it ultimately converges to the same fixed point, characterized by constant energy dissipation.

Note that after studying the effect of the numerical perturbation on the Jacobian Matrix calculation see Figure 3.3 it is concluded that the perturbation $\varepsilon = 1e-4$ is an adequate perturbation for the knee biped system developed.

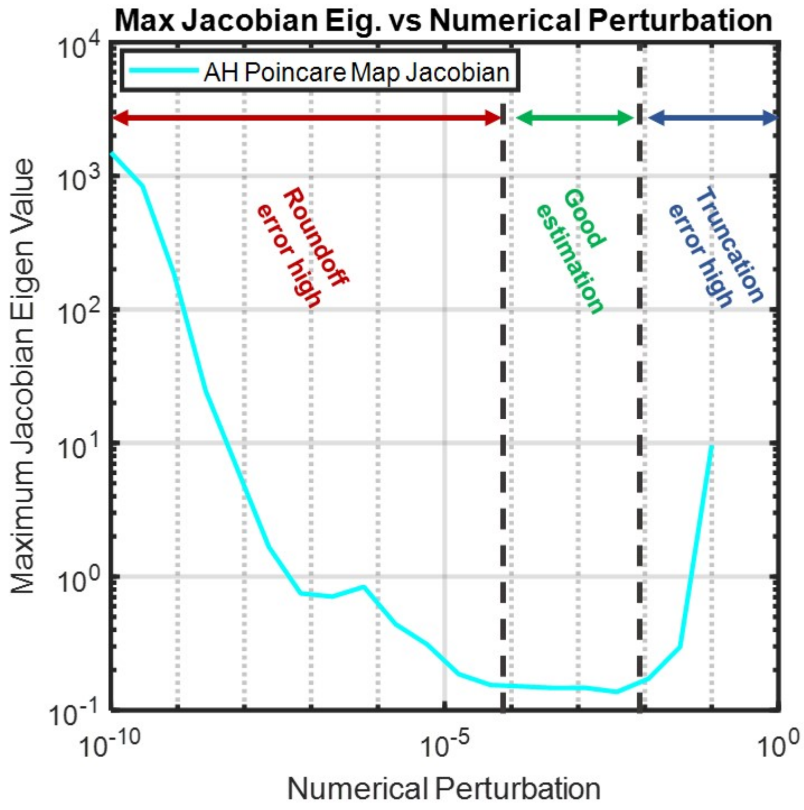

Figure 3.3: Maximum eigenvalue norm of the Jacobian matrix of the AH Poincare Map. Without loss of generality, the Jacobian is calculated at the fixed point of the Poincare Map. For small perturbations, the roundoff error gives a wrong estimation of the Jacobian while for big perturbations the Truncation error gives also a wrong estimation of the Jacobian. A good estimation of the Jacobian is obtained for perturbations between $[1e-4, 1e-2]$

$$\frac{\partial P_{AH}}{\partial \theta_K}|_{\hat{\mathbf{x}}=\hat{x}_a} = \frac{P_{AH}|_{\hat{\mathbf{x}}=\hat{x}_a+[\varepsilon/2,0,0,0,0,0,0]^\tau} - P_{AH}|_{\hat{\mathbf{x}}=\hat{x}_a-[\varepsilon/2,0,0,0,0,0,0]^\tau}}{\varepsilon} \tag{3.8}$$

The process of calculating the Jacobian matrix for the AH Poincare Map requires 14 Poincare Map evaluations. Each evaluation of the Poincare Map is a run of the sequence of the phases mentioned in equation 3.1 or 3.2 for the dynamic system characterized by nonlinear differential-algebraic equations. It is inferred that the computation cost for the Jacobian calculation is high enough. Although some tricks can be done in order to reduce the computation cost of the Jacobian calculation.

During the optimization, the model is considered symmetric in order to reduce optimization parameters to half. The symmetry of the model enables the possibility to express the gait using the sequence 3.2 the same sequence can be written in the form of equation 3.9. Note that this sequence consists of the sequence of 2 semi-gaits. This means that there is the possibility of studying the semi-gait model rather than the whole gait. This action reduces the dynamic model simulation time to half and offers the capability of studying highly unstable biped that during their second half of the gait would fall terminating the gait simulations. So the sequence of the phases that will be simulated is presented in equation 3.10

$$SSP_1 \overset{HS_2}{\to} DSP \overset{TO_1}{\to} SSP_2 \overset{AH}{\to} (\theta \leftrightarrows \psi) SSP_1 \overset{HS_2}{\to} DSP \overset{TO_1}{\to} SSP_2 \overset{AH}{\to} (\theta \leftrightarrows \psi) \tag{3.9}$$

$$SSP_1 \overset{HS_2}{\to} DSP \overset{TO_1}{\to} SSP_2 \overset{AH}{\to} (\theta \leftrightarrows \psi) \tag{3.10}$$

Also, it is clear that when a foot is in stance the foot's knee is locked due to the existence of the knee cup. Even small disturbances in the knee joint, due to its high energy dissipating knee cup, are rapidly obliterated from the rest of the system. This means that the Poincare Map Jacobian can estimated without calculating the derivatives related to state variable $[\theta_K, \dot{\theta}_K]$. This fact can be proved using the example of calculation of the Jacobian matrix with and without them, see equation 3.11. Note that the number of partial derivatives calculated is reduced from 49 to 25.

$$\begin{aligned}
\nabla P_{AH}|_{\hat{x}=\hat{x}_a} &= \begin{bmatrix} 0.0786 & -0.1112 & -0.5491 & -0.2292 & 0.3383 \\ 0.3553 & -0.5018 & -0.3162 & -1.2099 & 1.7656 \\ -0.0419 & 0.0592 & 0.4752 & 0.1109 & -0.1653 \\ 0.9834 & -1.3896 & 0.0417 & -3.4020 & 4.9589 \\ 0.7037 & -0.9946 & 0.9224 & -2.4933 & 3.6267 \end{bmatrix} \\
\|eig(\nabla P_{AH}|_{\hat{x}=\hat{x}_a})\| &= \begin{bmatrix} 0.1512 & 0.1512 & 0.1495 & 0.0017 & 0.0001 \end{bmatrix} \\
\nabla P'_{AH}|_{\hat{x}=\hat{x}_a} &= \begin{bmatrix} -0.0007 & 0.0004 & -0.0006 & -0.0025 & 0.0030 & -0.0012 & 0.0018 \\ -0.1388 & 0.0786 & -0.1112 & -0.5491 & 0.6949 & -0.2292 & 0.3383 \\ -0.5925 & 0.3553 & -0.5018 & -0.3162 & -0.5920 & -1.2099 & 1.7656 \\ 0.0779 & -0.0419 & 0.0592 & 0.4752 & -0.6842 & 0.1109 & -0.1653 \\ 0.0019 & -0.0010 & 0.0014 & 0.0144 & -0.0216 & 0.0024 & -0.0036 \\ -1.6207 & 0.9834 & -1.3896 & 0.0417 & -3.2116 & -3.4020 & 4.9589 \\ -1.1416 & 0.7037 & -0.9946 & 0.9224 & -3.8317 & -2.4933 & 3.6267 \end{bmatrix} \\
\|eig(\nabla P'_{AH}|_{\hat{x}=\hat{x}_a})\| &= \begin{bmatrix} 0.1576 & 0.1576 & 0.1303 & 0.0017 & 0.0001 & 0.0000 & 0.0000 \end{bmatrix}
\end{aligned} \tag{3.11}$$

3.4 Fixed point of the AH Poincare Map

The calculation of the fixed point of the AH Poincare Map is crucial for the optimization process. The gait starting from the fixed point can be characterized firstly in terms of stability and secondly in terms of trajectory (e.g. period, gait step size, trajectory form). The fixed point is described by the following equation 3.12

To calculate the fixed point, the Newton-Raphson method is used see 3.14 as the method's effectiveness is irrelevant to the fixed point's stability. This fact gives, from an algorithmic point of view, robustness in the process of fixed point calculation which is very important for the next steps of this study.

$$
\begin{aligned}
P_{AH}(\hat{\hat{\mathbf{x}}}^*_{\mathbf{k}}) &= \hat{\hat{\mathbf{x}}}^*_{\mathbf{k}} \Rightarrow \\
P_{AH}(\hat{\hat{\mathbf{x}}}^*_{\mathbf{k}}) - \hat{\hat{\mathbf{x}}}^*_{\mathbf{k}} &= 0 \Rightarrow \\
G_{AH}(\hat{\hat{\mathbf{x}}}^*_{\mathbf{k}}) &= 0
\end{aligned} \tag{3.12}
$$

The fixed point expression can be simplified.

$$
\hat{\hat{\mathbf{x}}}^* = \hat{\hat{\mathbf{x}}}^*_{\mathbf{k}} = \hat{\hat{\mathbf{x}}}^*_{\mathbf{k+1}} \tag{3.13}
$$

The fixed point of the Poincare map is calculated iteratively starting from an initial guess $\hat{\hat{\mathbf{x}}}^{*<0>}$. The fixed point calculation process stops when the value $max(|G_{AH}(\hat{\hat{\mathbf{x}}}^{*<j>})|)$ stops dropping for a specific amount of iterations. Then it is inferred that the Newton-Raphson algorithm has converged. See Figure 3.4

$$
\begin{aligned}
\hat{\hat{\mathbf{x}}}^{*<j+1>} &= \hat{\hat{\mathbf{x}}}^{*<j>} - \nabla G_{AH}^{-1}|_{\hat{\hat{\mathbf{x}}}=\hat{\hat{\mathbf{x}}}^{*<j>}} \cdot G_{AH}(\hat{\hat{\mathbf{x}}}^{*<j>}) \Rightarrow \\
\hat{\hat{\mathbf{x}}}^{*<j+1>} &= \hat{\hat{\mathbf{x}}}^{*<j>} - \left[\nabla P_{AH}|_{\hat{\hat{\mathbf{x}}}=\hat{\hat{\mathbf{x}}}^{*<j>}} - eye(5)\right]^{-1} \cdot \left[P_{AH}(\hat{\hat{\mathbf{x}}}^{*<j>}) - \hat{\hat{\mathbf{x}}}^{*<j>}\right]
\end{aligned} \tag{3.14}
$$

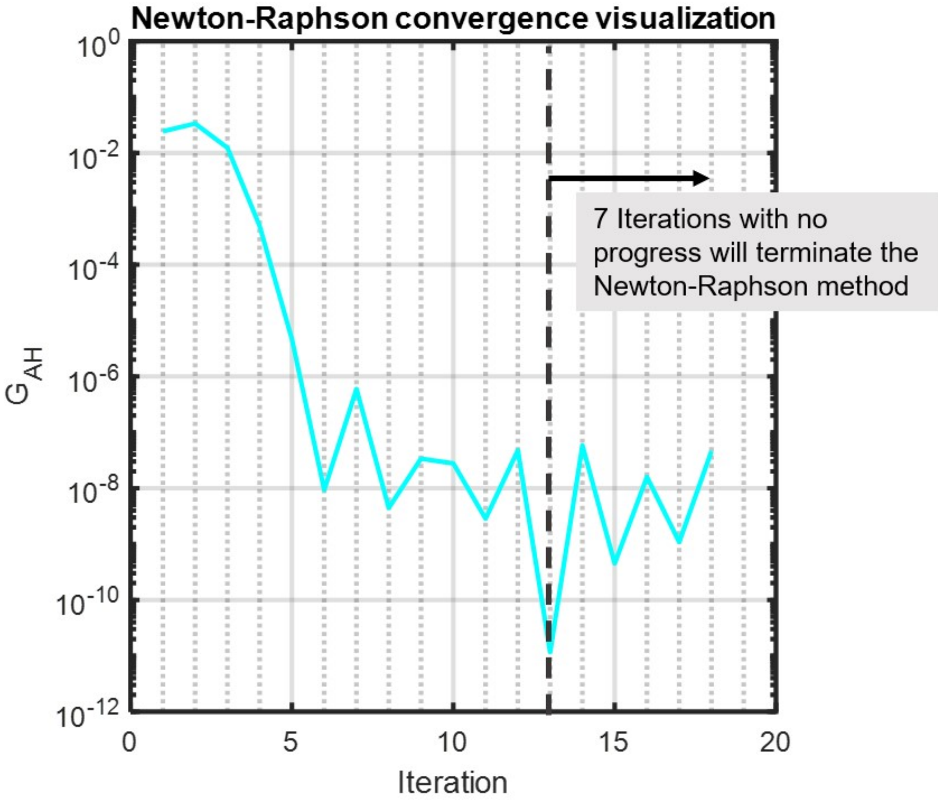

Figure 3.4: Newton Raphson algorithm convergence visualization. The algorithm begins from an estimation that is the fixed point perturbed randomly in a scale of $\pm 30\%$

4 Model Optimization

Prior to the design of a bipedal robot with knees, the focus of this work is to optimize the model parameters, ensuring that the robot exhibits a stable gait without any foot scuffing issues. It is imperative that the optimized parameters align with the feasibility of manufacturing the robot.

The optimization process is structured into three distinct phases. In the initial phase, optimization constraints are not taken into account. The second phase is a semi-constrained optimization step, where the most challenging aspect of the construction according to the first optimization phase, is designed. The parameters associated with this specific part are computed and held constant, while the parameters linked to the remaining components of the construction undergo another round of unconstrained optimization. The insights gained from the second optimization phase aid in the creation of a CAD model. The third and final phase of optimization utilizes an existing CAD model and is a constrained optimization. In this phase, the dimensional parameters of the model are allowed to deviate by up to $\pm 10\%$ from the CAD design parameters.

4.1 Introduction to the steepest descent

The optimization method is a gradient-based optimization. Specifically, the steepest descent method is used. The objective function $F(\vec{b})$ is composed of multiple objectives F_i multiplied by weights w_i that correspond to each optimization phase's needs and are added together see equation 4.1. The steepest descent method aims to reduce the value of F by moving the optimization parameters $\vec{b}$ to the direction that reduces the objective function's value see 4.2. To visualize the method's principles see Figure 4.1. The objective function gradients with respect to the optimization parameters are computed with finite differences.

The optimization approach employed in this study is based on gradient descent, specifically utilizing the steepest descent method. The objective function, denoted as $F(\vec{b})$, is a composite of various objectives F_i, each multiplied by respective weights w_i. These weights are tailored to the requirements of each optimization phase and are summed together, as indicated in Equation 4.1. The steepest descent method is employed to minimize the value of the objective function F by adjusting the optimization parameters $\vec{b}$ in a direction that leads to a reduction in the objective function value, as illustrated in Equation 4.2. For a more visual explanation of the method's principles, refer to Figure 4.1. The gradients of the objective function with respect to the optimization parameters are computed using finite differences, see Equation4.3.

$$F = \sum_{i=1}^{nf} w_i \cdot F_i \tag{4.1}$$

$$\vec{b}^{new} = \vec{b}^{old} - \eta \cdot \frac{dF}{d\vec{b}}|_{\vec{b}=\vec{b}^{old}} \tag{4.2}$$

$$\frac{\partial F}{\partial b_i} = \frac{F_{front} - F_{back}}{\varepsilon_b} \tag{4.3}$$

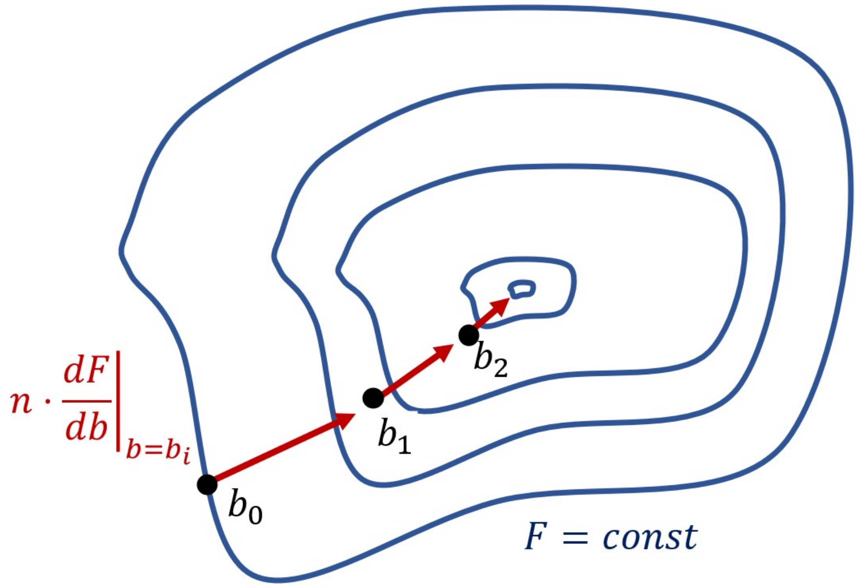

Figure 4.1: Visualization of the steepest descent optimization method working principle

4.2 Implementation of the steepest descent to AH Poincare Map

The steepest descent method is chosen for this specific optimization case due to a particular reason. As explained in subsection 3.4, when there is need to find the fixed point of the Poincare maps (which corresponds to a specific set of parameters), the Newton-Raphson method is used. This method requires an initial guess to start its calculations. To make this initial guess for the next set of optimization parameters $\vec{b}_{i+1}$ in the next optimization iteration $(i+1)$, the fixed point found in the previous optimization iteration (i) with optimization parameters $\vec{b}_i$ can be used.

The steepest descend algorithm outline is the following. The initial model parameters b_0 are specified. Then the fixed point that corresponds to these parameters is calculated. At this point, the following procedure takes place. For each optimization parameter, a positive perturbation ε_b is applied producing a perturbed set of parameters. The fixed point that corresponds to the new set of parameters is calculated then the objective function value F_{front} is calculated. The objective function depends on the characteristics of the model parameters, the Poincare Map at the fixed point, and the trajectory of the limit cycle of the biped. The same procedure is also done with a negative perturbation of the optimization parameter. The objective function's value is called F_{back}. The gradient of the objective function with respect to the optimization parameter is calculated with central differences see equation 4.3. When all the partial derivatives of the objective function for each design parameter have been calculated, the equation 4.2 is applied in order to calculate the new design parameters. The procedure can be visualized via the following block diagram 4.2.

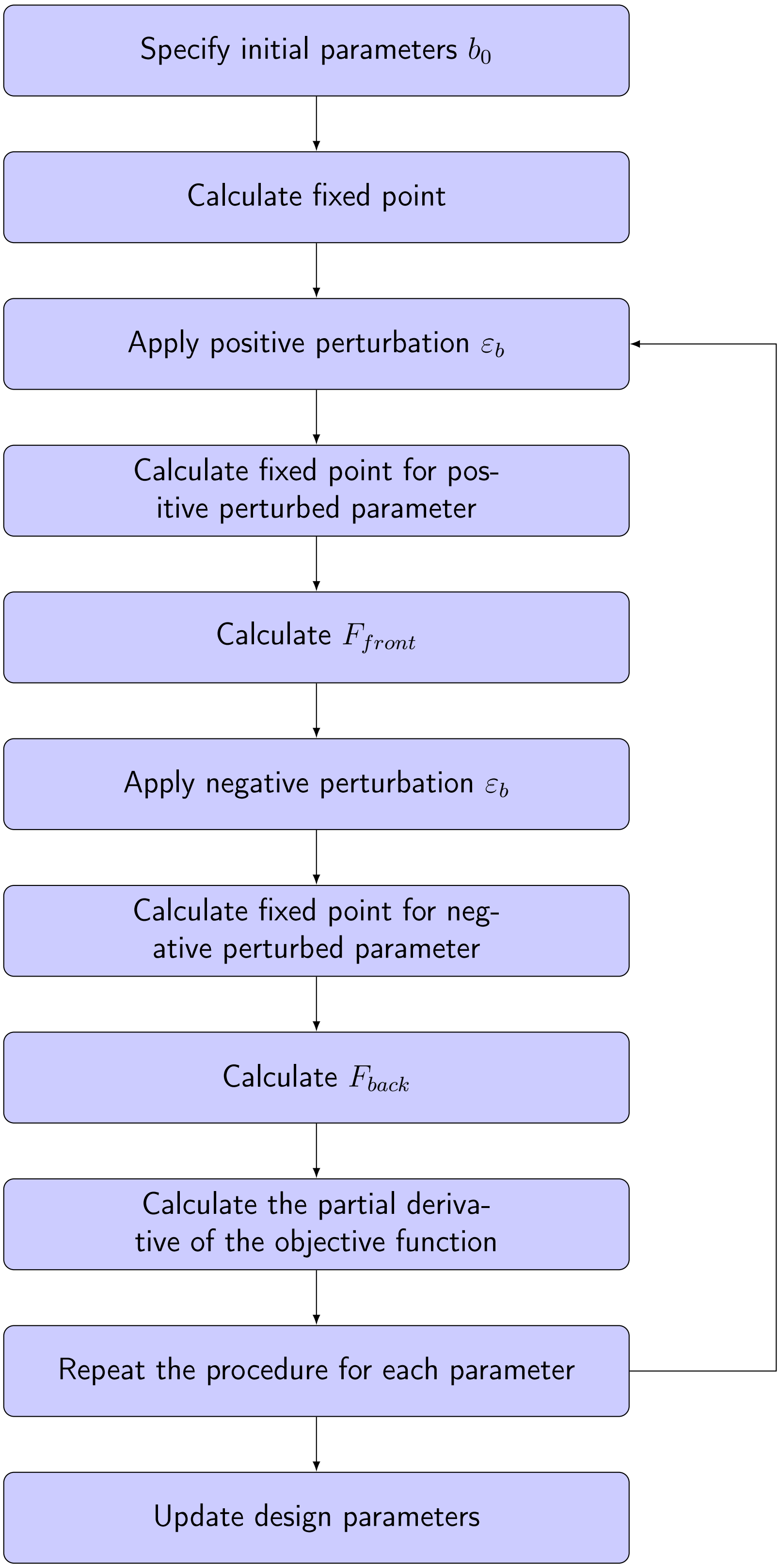

Figure 4.2: Block diagram the steepest descend algorithm outline.

4.3 Steepest descend objective function

As mentioned above the steepest objective function is composed of the sum of objective functions multiplied by a weight see equation 4.1. In this section each one of the sub-objective functions will be explained.

4.3.1 Maximum eigenvalue

The maximum eigenvalue of each of the Jacobian of the Poincare map at a fixed point is a metric of the decay or growth rate of a disturbance applied to the fixed point state.

Although the methodology for specifying the maximum Jacobian eigenvalue is straightforward see equation 4.4 according to the section. The specific dynamic model of the biped is hybrid and governed by nonlinear differential-algebraic equations. The algorithm of calculating the maximum eigenvalue norm of the Jacobian at the fixed point operates with highly chaotic behavior.

The need to obtain a more deterministic metric of the fixed point stability emerges. In order to achieve that, during the calculation of the fixed point algorithm see section 3.4, the Jacobian matrices of the top 5 ($j = 1 : 5$) fixed point estimations are collected. For each Jacobian matrix j the maximum eigenvalue norm of the Jacobian $\lambda_{max,j}$ is calculated. Then the mean value $\bar{\lambda}_{max}$ is calculated see equation 4.5. The objective function related to the stability of at the fixed point F_λ is calculated according to the equation 4.6.

$$\lambda_{max} = max(\|eig(\nabla P_{AH}\|)) \tag{4.4}$$

$$\bar{\lambda}_{max} = \frac{\sum_{j=1}^{5} \lambda_{max,j}}{5} \tag{4.5}$$

$$F_\lambda = \bar{\lambda}_{max} \tag{4.6}$$

4.3.2 Minimum distance from scuffing

From previous research, it is evident that when experimentally evaluating passive kneed bipeds, one of the most common causes of failure in achieving stable walking is foot scuffing during the swing phase of the leg that is in flight. Therefore, this study aims to minimize the likelihood of foot scuffing.

The metric of the possibility of the foot to scuff is the minimum distance between the swing leg from the ground during the swing phase of the leg at the fixed point. To achieve that, the trajectory of the limit cycle is calculated at the fixed point $\mathbf{x}^*(t)$. An algorithm $D_{min}(\mathbf{x}^*(t))$ that calculates the minimum distance d_{min} between the foot and the ground through the limit cycle has been developed see equation 4.7. The objective function related to the foot scuffing at the fixed point $F_{d_{min}}$ is defined according to equation 4.8. The algorithm's capability of finding the minimum foot clearance can be verified with figure 4.3.

$$d_{min} = D_{min}(\mathbf{x}^*(t)) \tag{4.7}$$

$$F_{d_{min}} = \frac{1}{d_{min}} \tag{4.8}$$

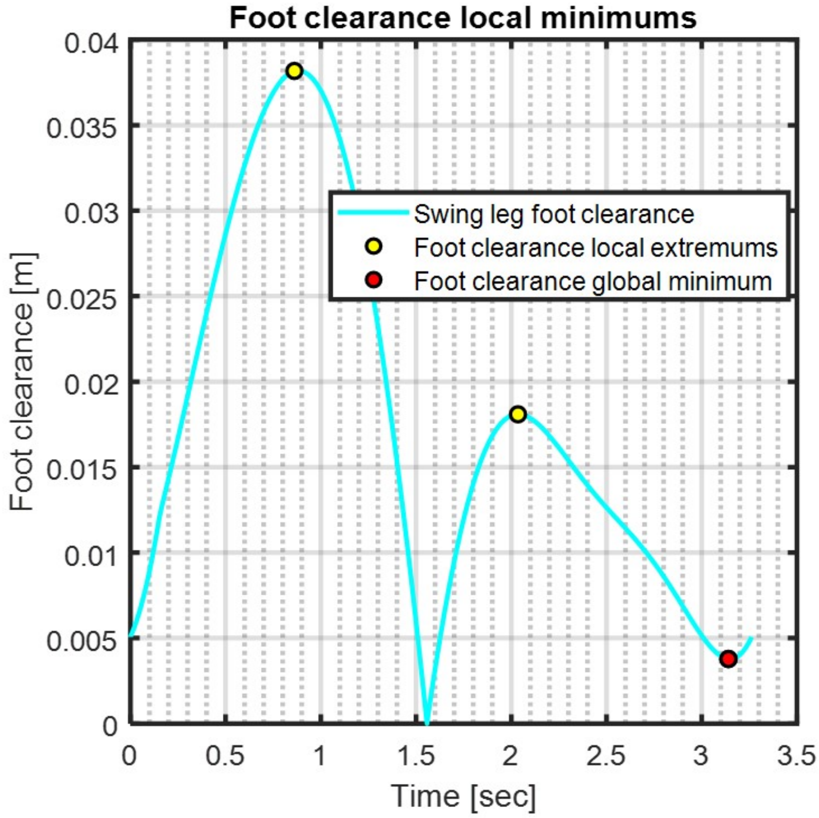

Figure 4.3: Foot clearance of the swing foot in a limit cycle. An algorithm for detecting the foot's clearance local extremums and the minimum foot clearance has been created

4.3.3 Deviation from CAD constraints cost function

The final objective function that will be used in this study, is the optimization model deviation from the CAD model parameters. In order to evaluate this cost function an existing CAD model must be available.

Note that the link lengths (L_F, L_T) and the hip's mass (M) are not inserted from the CAD model. During the construction constraints calculation, those inputs are inserted from the optimization model values and the CAD parameters change accordingly. This means that the cost function will be a function of the following optimization model parameters (L_{Tot}, L_F^* and M^*) and the construction characteristics that are provided by CAD and are presented in the next paragraph.

Inputs for construction constraints calculation from CAD

The femoral link structure ($Fem^{h.c.}$) connects to the hip joint structure with the femoral link, as depicted in Figure 4.4. The relevant inertial characteristics of this structure include the center of mass distance from the upper femoral link point in the link-wise axis direction ($Fem_l^{h.c.}$), the center of mass distance from the upper femoral link point in the link-wise axis transversal direction

($Fem_{lx}^{h.c.}$), the mass ($Fem_{m}^{h.c}$), and the moment of inertia about the structure's center of mass ($Fem_{I_{xx}}^{h.c}$).

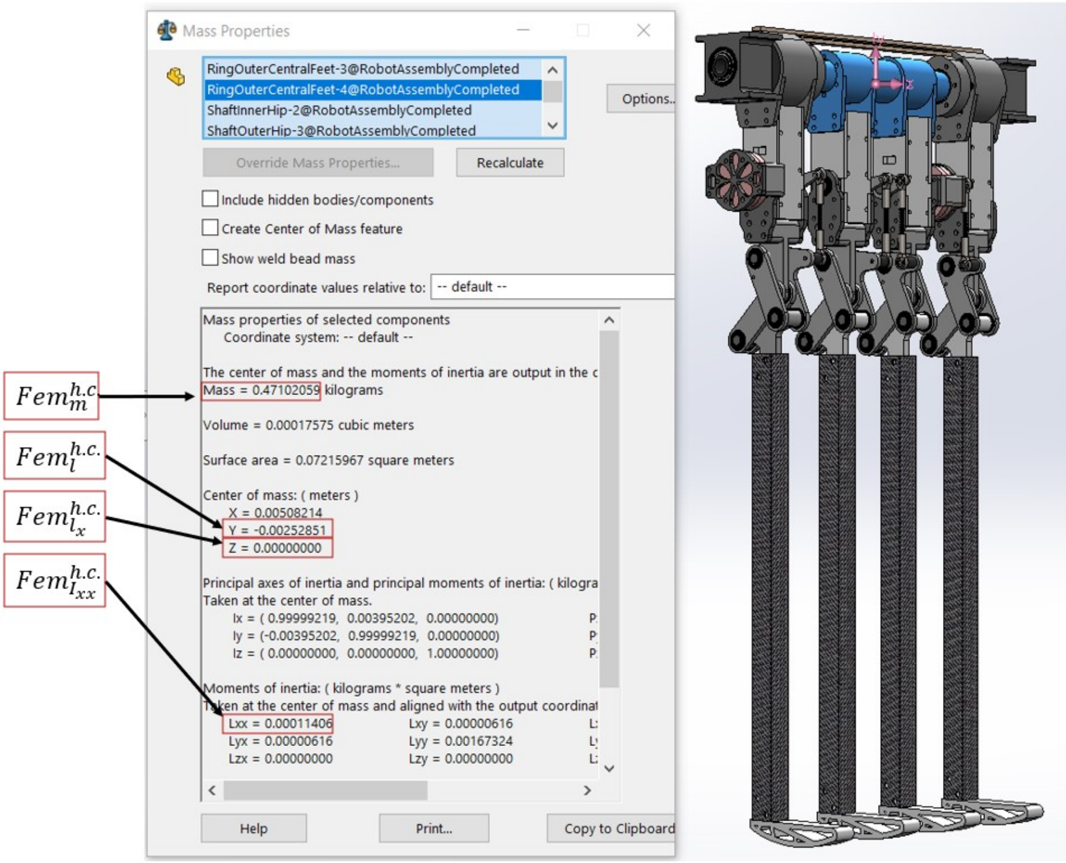

Figure 4.4: $Fem^{h.c.}$ structure inertial characteristics provided from CAD

The femoral link structure ($Fem^{k.c.}$) connects the femoral with the knee joint and is illustrated in Figure 4.5. The relevant inertial characteristics of this structure encompass the center of mass distance from the lower femoral link point in the link-axis direction ($Fem_{l}^{k.c.}$), the center of mass distance from the lower femoral link point in the link-axis transversal direction ($Fem_{lx}^{k.c.}$), the mass ($Fem_{m}^{k.c.}$), and the moment of inertia measured about the center of mass of the $Fem^{k.c.}$ structure ($Fem_{I_{xx}}^{k.c.}$).

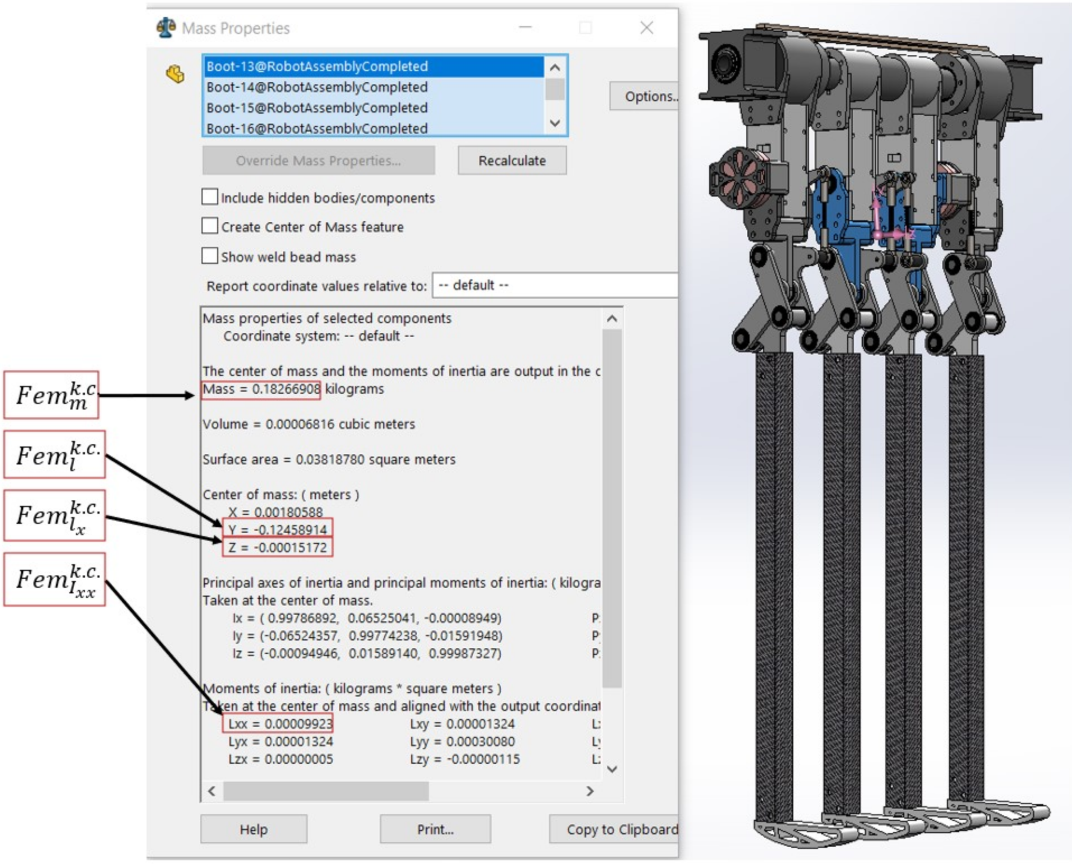

Figure 4.5: $Fem^{k.c.}$ structure inertial characteristics provided from CAD

The tibial link structure ($Tib^{k.c.}$) connects the tibial beam to the knee joint and is illustrated in Figure 4.6. The relevant inertial characteristics of this structure include the center of mass distance from the upper tibial link point in the link-axis direction ($Tib_l^{k.c.}$), the center of mass distance from the upper tibial link point in the link-axis transversal direction ($Tib_{lx}^{k.c.}$), the mass ($Tib_m^{k.c.}$), and the moment of inertia measured about the center of mass of the $Tib^{k.c.}$ structure ($Tib_{I_{xx}}^{k.c.}$).

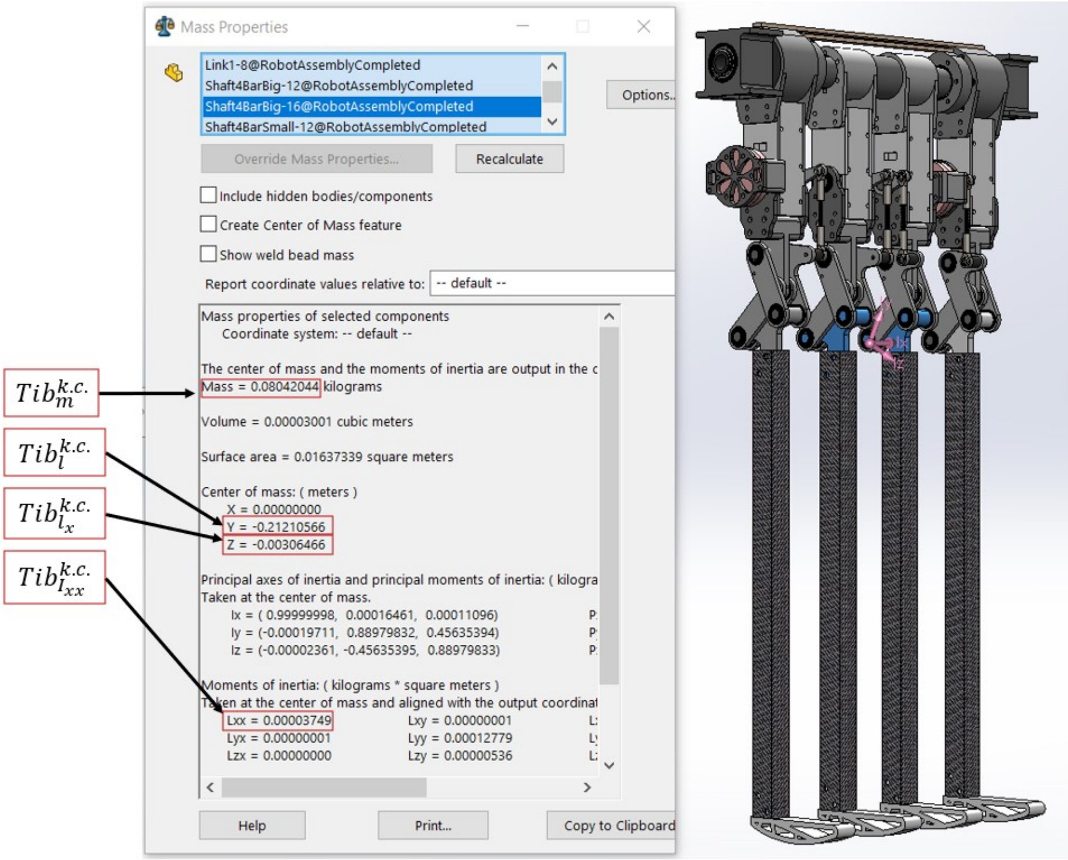

Figure 4.6: $Tib^{k.c.}$ structure inertial characteristics provided from CAD

The foot limb structure ($Tib^{f.l.}$) is connected to the tibial beam, as shown in Figure 4.7. The relevant inertial characteristics of this structure include the center of mass distance from the lower tibial link point in the link-axis direction ($Tib_l^{f.l.}$), the center of mass distance from the lower tibial link point in the link-axis transversal direction ($Tib_{lx}^{f.l.}$), the mass ($Tib_m^{f.l.}$), and the moment of inertia measured about the center of mass of the $Tib^{f.l.}$ structure ($Tib_{I_{xx}}^{f.l.}$).

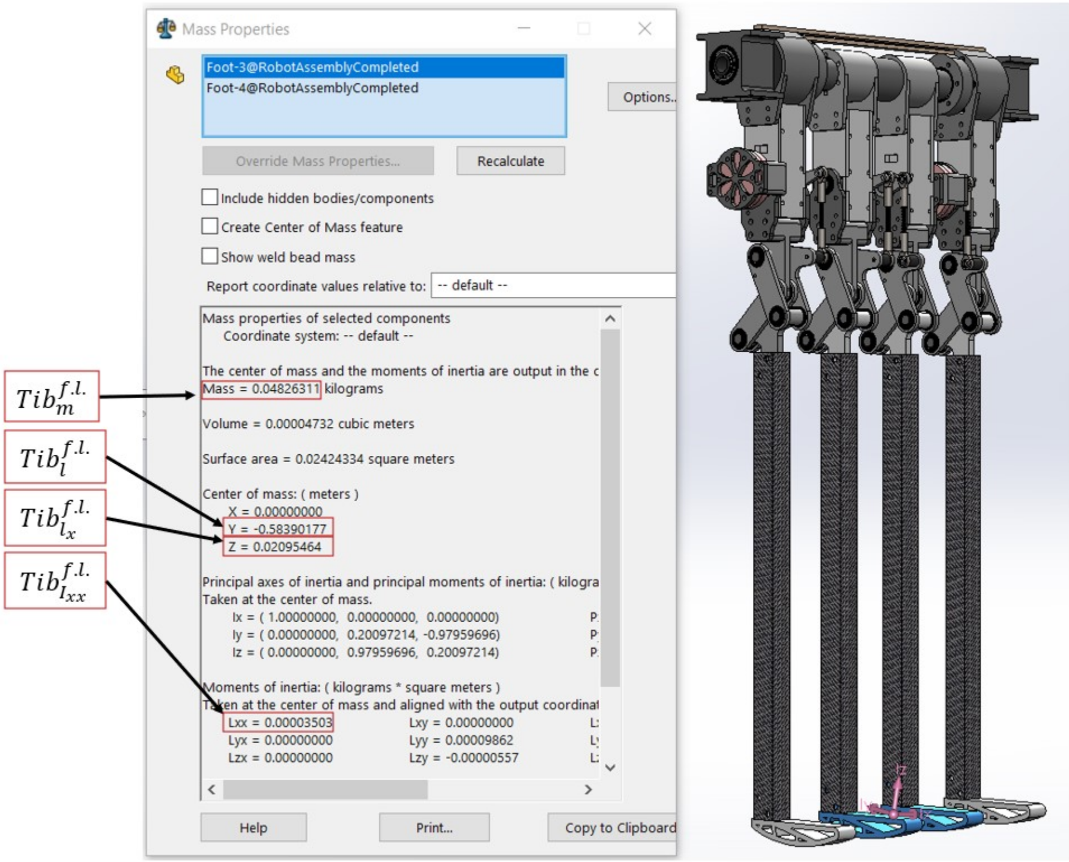

Figure 4.7: Tibial link's foot limb inertial characteristics provided from CAD

Furthermore, cross-section data for the femoral beam are provided. In the case of a squared cross-section, the following parameters are used: inner width ($Fem_{w.i.}^{c.s.}$), inner depth ($Fem_{d.i.}^{c.s.}$), outer width ($Fem_{w.o.}^{c.s.}$), and outer depth ($Fem_{d.o.}^{c.s.}$). These parameters are illustrated in Figure 4.8.

In addition to this, we consider certain distance measurements: the distance between the CAD femoral beam's upper point and the theoretical femoral link's upper point (in the link-wise direction) is denoted as $Fem^{u.dist}$, the distance between the CAD femoral beam's lower point and the theoretical femoral link's lower point (in the link-wise direction) is symbolized as $Fem^{l.dist}$, and the distance between the CAD cross-section center of the femoral beam and the theoretical femoral link's upper point (in the transverse direction to the link-wise axis) is represented as $Fem^{cs.dist_x}$. You can refer to Figure 4.9 for a visual representation of these distances.

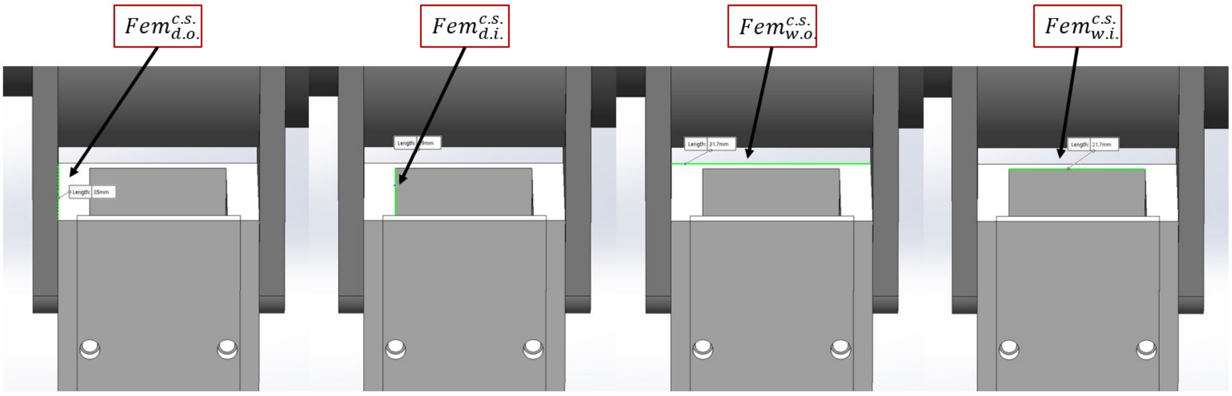

Figure 4.8: Femoral hollow square cross-section data provided from CAD

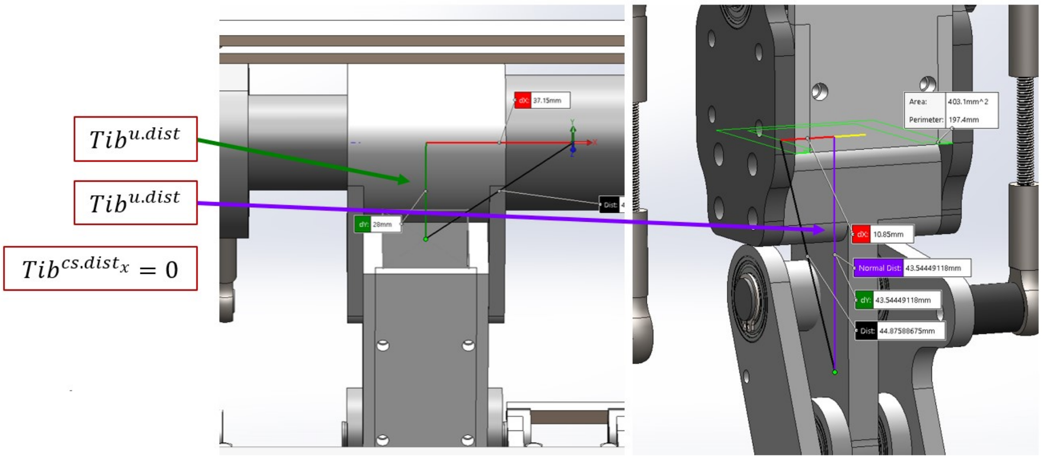

Figure 4.9: CAD femoral beam distances from the theoretical femoral link.

In a similar manner, cross-section data for the tibial beam are provided. When considering a squared cross-section, we use the following parameters: inner width ($Tib^{c.s.}_{w.i.}$), inner depth ($Tib^{c.s.}_{d.i.}$), outer width ($Tib^{c.s.}_{w.o.}$), and outer depth ($Tib^{c.s.}_{d.o.}$). These parameters are visually represented in Figure 4.10.

Additionally, we take into account specific distance measurements: the distance between the CAD tibial beam's upper point and the theoretical tibial link's upper point (in the link-wise direction) is denoted as $Tib^{u.dist}$, the distance between the CAD tibial beam's lower point and the theoretical tibial link's lower point (in the link-wise direction) is symbolized as $Tib^{l.dist}$, and the distance between the CAD cross-section center of the tibial beam and the theoretical tibial link's upper point (in the transverse direction to the link-wise axis) is represented as $Tib^{cs.dist_x}$. Figure 4.11 provides a visual overview of these distances.

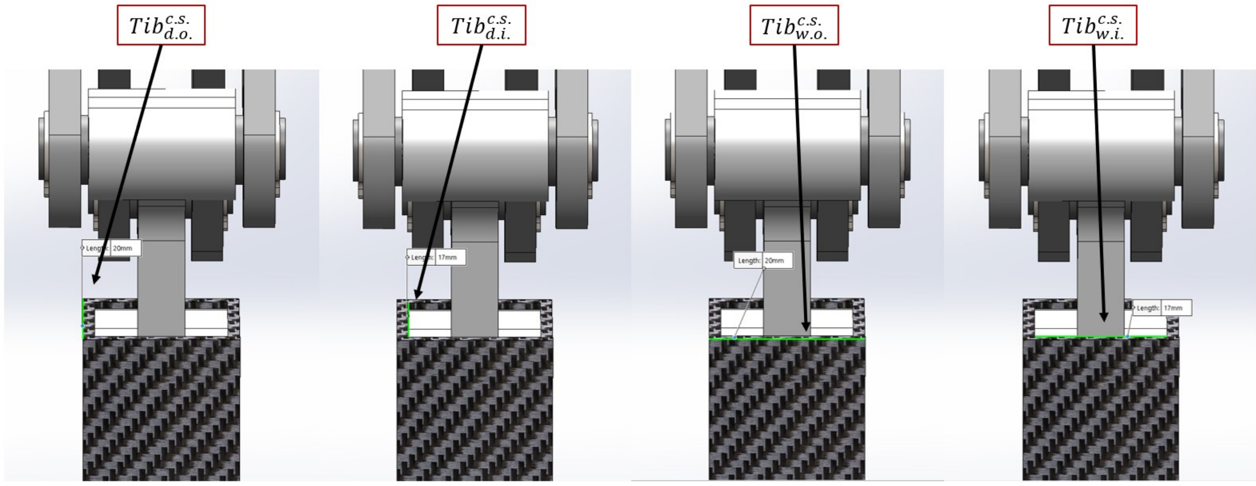

Figure 4.10: Tibial hollow square cross-section data provided from CAD

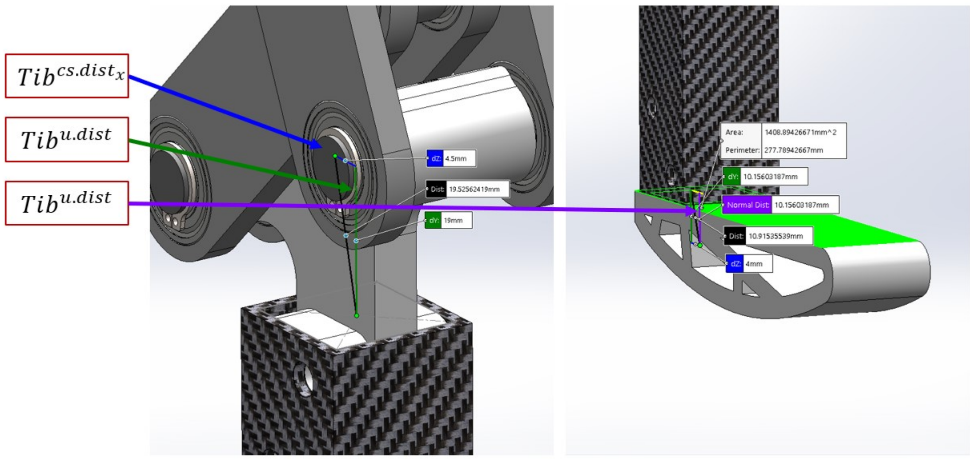

Figure 4.11: CAD tibial beam distances from the theoretical tibial link.

Construction constraints calculation

The initial step in the construction constraints calculation process involves determining the construction characteristics of the femoral and tibial beams. We begin by calculating the CAD link lengths (L_F^{link},L_T^{link}) using the formula provided in equation 4.9. Subsequently, we compute the CAD beam lengths (L_F^{beam} and L_T^{beam}) as per equation 4.10.

Furthermore, the cross-section areas ($Fem_A^{c.s.}$ and $Tib_A^{c.s.}$) of the tibial and femoral CAD beams are determined, as described in equation 4.11. We proceed to calculate the mass (m_F^{beam},m_T^{beam}), the inertia (I_F^{beam},I_T^{beam}), and the center of mass related to the upper point of the theoretical links (l_F^{beam},lx_F^{beam},l_T^{beam},lx_T^{beam}) according to the equation in 4.12.

$$\begin{aligned} L_F^{link} &= L_F' \cdot L_{tot} \\ L_T^{link} &= L_{tot} - L_F^{link} \end{aligned} \tag{4.9}$$

$$
\begin{aligned}
L_F^{beam} &= L_F^{link} - Fem^{u.dist} - Fem^{l,dist} \\
L_T^{beam} &= L_T^{link} - Tib^{u.dist} - Tib^{l,dist}
\end{aligned} \tag{4.10}
$$

The cross-section area is calculated. Note that the area calculated is multiplied by 2. This happens as each leg is constructed from 2 rectangular beams.

$$
\begin{aligned}
Fem_A^{c.s.} &= (Fem_{d.o}^{c.s.} \cdot Fem_{w.o}^{c.s.} - Fem_{d.i}^{c.s.} \cdot Fem_{w.i}^{c.s.}) \cdot 2 \\
Tib_A^{c.s.} &= (Tib_{d.o}^{c.s.} \cdot Tib_{w.o}^{c.s.} - Tib_{d.i}^{c.s.} \cdot Tib_{w.i}^{c.s.}) \cdot 2
\end{aligned} \tag{4.11}
$$

$$
\begin{aligned}
m_F^{beam} &= Fem_A^{c.s.} \cdot L_F^{beam} \cdot \rho_F \\
m_T^{beam} &= Tib_A^{c.s.} \cdot L_T^{beam} \cdot \rho_T \\
I_F^{beam} &= m_F^{beam} \cdot \frac{L_F^{beam^2}}{12} \\
I_T^{beam} &= m_T^{beam} \cdot \frac{L_T^{beam^2}}{12} \\
l_F^{beam} &= Fem^{u.dist} + \frac{L_F^{beam}}{2} \\
l_T^{beam} &= Tib^{u.dist} + \frac{L_T^{beam}}{2} \\
lx_F^{beam} &= Fem^{cs.dist_x} \\
lx_T^{beam} &= Tib^{cs.dist_x}
\end{aligned} \tag{4.12}
$$

The CAD link inertial characteristics calculation procedure is recursive with the initial link characteristics to be the same as the beam inertial characteristics calculated before see equation 4.13. For the femoral link, the $Fem^{h.c.}$ structure is added initially while for the tibial link, the $Tib^{k.c.}$ structure is added see equation 4.14. Continuously for the femoral, the $Fem^{k.c.}$ structure is added while for the tibial link, the $Tib^{f.l.}$ structure is added, see equation 4.15.

$$
\begin{aligned}
m_F^{link} &= m_F^{beam} \\
m_T^{link} &= m_T^{beam} \\
l_F^{link} &= l_F^{beam} \\
l_T^{link} &= l_T^{beam} \\
lx_F^{link} &= lx_F^{beam} \\
lx_T^{link} &= lx_T^{beam} \\
I_F^{link} &= I_F^{beam} \\
I_T^{link} &= I_T^{beam}
\end{aligned}
\tag{4.13}
$$

$$
\begin{aligned}
m_F^{link'} &= m_F^{link} + Fem_m^{h.c} \\
m_T^{link'} &= m_T^{beam} + Tib_m^{k.c} \\
l_F^{link'} &= \frac{m_F^{link} \cdot l_F^{link} + Fem_m^{h.c} \cdot Fem_l^{h.c}}{m_F^{link} + Fem_m^{h.c}} \\
l_T^{link'} &= \frac{m_T^{link} \cdot l_T^{link} + Tib_m^{k.c} \cdot Tib_l^{k.c}}{m_T^{link} + Tib_m^{k.c}} \\
lx_F^{link'} &= \frac{m_F^{link} \cdot lx_F^{link} + Fem_m^{h.c} \cdot Fem_{lx}^{h.c}}{m_F^{link} + Fem_m^{h.c}} \\
lx_T^{link'} &= \frac{m_T^{link} \cdot lx_T^{link} + Tib_m^{k.c} \cdot Tib_{lx}^{k.c}}{m_T^{link} + Tib_m^{k.c}} \\
I_F^{link'} &= I_F^{link} + |l_F^{link'} - l_F^{link}|^2 \cdot m_F^{link} + |l_F^{link'} - Fem_l^{h.c}|^2 \cdot Fem_m^{h.c} \\
I_T^{link'} &= I_T^{link} + |l_T^{link'} - l_T^{link}|^2 \cdot m_T^{link} + |l_T^{link'} - Tib_l^{k.c}|^2 \cdot Tib_m^{k.c}
\end{aligned}
\tag{4.14}
$$

$$
\begin{aligned}
m_F^{link''} &= m_F^{link'} + Fem_m^{k.c} \\
m_T^{link''} &= m_T^{beam} + Tib_m^{f.l} \\
l_F^{link''} &= \frac{m_F^{link'} \cdot l_F^{link'} + Fem_m^{k.c} \cdot (L_F^{link} - Fem_l^{k.c})}{m_F^{link'} + Fem_m^{k.c}} \\
l_T^{link''} &= \frac{m_T^{link'} \cdot l_T^{link'} + Tib_m^{f.l} \cdot (L_T^{link} - Tib_l^{f.l})}{m_T^{link'} + Tib_m^{f.l}} \\
lx_F^{link''} &= \frac{m_F^{link'} \cdot lx_F^{link'} + Fem_m^{k.c} \cdot Fem_{lx}^{k.c}}{m_F^{link'} + Fem_m^{k.c}} \\
lx_T^{link''} &= \frac{m_T^{link'} \cdot lx_T^{link'} + Tib_m^{f.l} \cdot Tib_{lx}^{f.l}}{m_T^{link'} + Tib_m^{f.l}} \\
I_F^{link''} &= I_F^{link'} + |l_F^{link''} - l_F^{link'}|^2 \cdot m_F^{link'} + |l_F^{link''} - (L_F^{link} - Fem_l^{k.c})|^2 \cdot Fem_m^{k.c} \\
I_T^{link''} &= I_T^{link'} + |l_T^{link''} - l_T^{link'}|^2 \cdot m_T^{link'} + |l_T^{link''} - (L_T^{link} - Tib_l^{f.l})|^2 \cdot Tib_m^{f.l}
\end{aligned} \tag{4.15}
$$

Now all the tibial and femoral link CAD inertial characteristics have been calculated. The next step of the procedure is the total mass calculation, see equation 4.16.

$$
\begin{aligned}
m_{tot} &= M + 2 \cdot m_F + 2 \cdot m_T \Rightarrow \\
m_{tot} &= M^* \cdot m_{tot} + 2 \cdot m_F + 2 \cdot m_T \Rightarrow \\
m_{tot} &= \frac{2 \cdot m_F + 2 \cdot m_T}{1 - M^*}
\end{aligned} \tag{4.16}
$$

Model parameters dimensionalization and construction deviation cost

At this point, all the CAD link inertial data are known. Also, the total mass and the total length of the robot are known. The next step of the method is the model inertial data dimensionalization based on the total mass, the total length, and the earth's gravitational acceleration. The dimensionalization of the non-dimensional model parameters is executed according to the table 2.1.

For each of the $i = 8$ CAD dimensional parameters ($m_F^{link''}, m_T^{link''}$, etc.), a range spanning $\pm 10\%$ around its central value, denoted as $bspan^{link}i$ (as shown in equation 4.17), is established. This range is considered the acceptable span for dimensional model parameters. If a dimensional model inertial parameter, denoted as bi, deviates from the corresponding span by a distance $dist(b_i, bspan_i^{link})$, the construction objective function value increases by the deviation distance multiplied by a specific weight, as indicated in equation 4.18.

$$
bspan_i^{link} = [b_i^{link} \cdot 0.9 - 0.005, b_i^{link} \cdot 1.1 + 0.005] \tag{4.17}
$$

$$F_{costruction} = \sum_{i=1}^{8} dist(b_i, bspan_i^{link}) \cdot w_{b_i} \tag{4.18}$$

Total mass cost

In general, it is important for the design process, that the total mass of the biped be kept limited. Lower mass in general means, less loading on the structural components of the biped and lower power demand for the active robot design. That means that a lighter construction is considered more cost-effective and it should be preferred.

In order to achieve that, a target mass m_{target} can be considered, and the deviation from the target mass multiplied by a weight w_{mass} can define a mass objective function. 4.19

$$F_{mass} = |m_{tot} - m_{target}|^{1.1} \tag{4.19}$$

4.4 Steepest descent optimization process

In the following subsection, the three optimization phases will be explained and described in more detail and the results from them will be presented and analyzed. The optimization process is focused on the following biped model's parameters (L_F^*, l_F^*, l_T^*, lx_T^*, m_F^*, m_T^*, I_F^* and I_T^*). Note that not all the parameters will be optimized in each optimization phase.

4.4.1 First optimization - unconstrained model parameters

The initial optimization process commences with a randomized set of model parameters, which typically yields an inherently unstable biped configuration. This optimization procedure operates without any constraints and employs two primary objective functions, namely $F_{\bar{\lambda}}$ and $F_{d_{min}}$. It is important to underscore that this optimization is primarily experimental in nature, designed to offer valuable insights into the extremities of the model's capabilities and the resulting model parameters.

Prior to the determination of each weight value, a sensitivity analysis is conducted to ascertain the appropriate weight values, as summarized in Table 4.1. Subsequently, based on the sensitivity evaluation, the weight assigned to the maximum eigenvalue objective is set to 1 ($w_{\bar{\lambda}} = 1$), and the weight for the minimum foot clearance is established at 5×10^{-4} ($w_{b_{min}} = 5 \times 10^{-4}$). The optimization parameters will be the following: L_F, lF, l^*T, m_F, mT, I^*F, and I_T^*.

As the optimization process is not expected to be convex, three gradient-based optimizations were executed, each commencing with different initial parameters:"Opt_{In1}", "Opt_{In2}", and"Opt_{in3}". The three different optimizations were terminated at distinct sets of parameters. Of course, the set of parameters corresponding to the best optimization results "Opt_{In1}" was chosen to continue the process. The "Opt_{In1}" gradient-based optimization was executed over the course of 20 optimization steps. As illustrated in Figure 4.12, it is evident that the optimization process displayed rapid convergence within the initial 7 steps. Subsequently, the rate of progress diminished significantly, prompting the termination of the optimization.

A comparison of the parameters before and after the optimization can be found in Table 4.3, allowing for an assessment of the modifications. Additionally, Table 4.4 presents a comparative analysis of the relevant metrics both before and after the optimization process.

b	$\frac{\delta \nabla F_{\bar{\lambda}}}{\delta b}$	$\frac{\delta \nabla F_{d_{min}}}{\delta b}$
L_F^*	-25.6621	0.6109·1e4
l_F^*	-11.2318	-0.1545·1e4
l_T^*	19.0996	-0.1422·1e4
m_F^*	-31.9156	-1.0295·1e4
m_T^*	19.8140	-4.4556·1e4
I_F^*	0.1374	0.2765·1e4
I_T^*	0.6431	-0.3096·1e4

Table 4.1: First optimization sensitivities

b	**Before the optimization**	**After the first optimization**	**Difference**
L_F^*	0.3032	0.2968	-0.0064
l_F^*	0.2565	0.2659	+0.0094
l_T^*	0.5525	0.5512	-0.0012
m_F^*	0.0305	0.0562	+0.0258
m_T^*	0.0304	0.0129	-0.0175
I_F^*	0.1500	0.1441	-0.0059
I_T^*	0.2574	0.2658	+0.0085

Table 4.2: Optimization parameters before and after the first optimization

b	Before The Optimization			After The Optimization			Before & After Difference		
	Opt_{In1}	Opt_{In2}	Opt_{In3}	Opt_{In1}	Opt_{In2}	Opt_{In3}	Opt_{In1}	Opt_{In2}	Opt_{In3}
L_F^*	0.3032	0.4245	0.4548	0.2968	0.3909	0.4222	-0.0064	-0.0022	-0.0639
l_F^*	0.2565	0.2565	0.2565	0.2659	0.2488	0.2451	0.0094	-0.0114	-0.0077
l_T^*	0.5525	0.6525	0.3525	0.5512	0.3326	0.6608	-0.0012	0.0083	-0.0199
m_F^*	0.0305	0.0610	0.0457	0.0562	0.0500	0.0620	0.0258	0.0010	0.0043
m_T^*	0.0304	0.0396	0.0304	0.0129	0.0823	0.0260	-0.0175	-0.0135	0.0519
I_F^*	0.1500	0.0750	0.1500	0.1441	0.1505	0.0754	-0.0059	0.0004	0.0005
I_T^*	0.2574	1.0295	0.5148	0.2658	0.5277	1.0343	0.0085	0.0048	0.0130

Table 4.3: Optimization parameters before and after the first optimization

Metric	Before The Optimization			After The Optimization			Before & After Difference		
	Opt_{In1}	Opt_{In2}	Opt_{In3}	Opt_{In1}	Opt_{In2}	Opt_{In3}	Opt_{In1}	Opt_{In2}	Opt_{In3}
$\bar{\lambda}_{max}$	1.0023	0.6185	0.4982	0.3054	0.2787	0.5550	-0.6969	-0.3398	-0.0568
$d_{min}[m]$	0.0017	0.0056	0.0002	0.0070	0.0061	0.0048	0.0053	0.0005	0.0046

Table 4.4: Metrics of interest before and after the first optimization

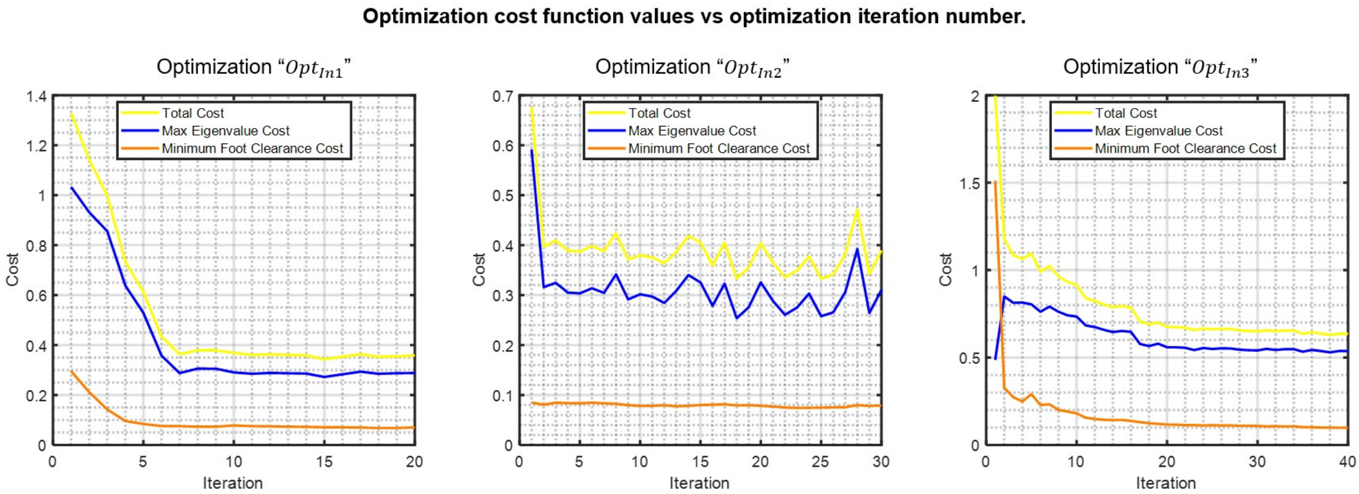

Figure 4.12: The unconstrained optimization comprises the initial phase of the optimization procedure. Multiple unconstrained optimizations, initiated with different sets of initial parameters, are presented. To ensure a fair comparison, optimization parameters such as weights are kept constant across the three optimizations. The final cost and convergence speed exhibit variations based on the initial model parameters. Each optimization converges to a local minimum of the cost function, indicating the non-convex nature of the cost function. Despite being non-convex, all local minima exhibit favorable stability metrics and a significant minimum distance between the swing leg and the ground. The optimization denoted as "Opt_{In1}" is chosen due to its lower total cost.

4.4.2 Second optimization - semi-constrained model parameter

Analysis of the results from the initial optimization reveals that the design and construction of the tibial link will pose particular challenges. The optimal solution indicates the importance of maintaining a relatively high value for its normalized length ($l_T^* = 1 - l_F = 0.7032$), while simultaneously keeping its normalized weight relatively small ($m_T^* = 0.0129$).

To realize this design objective, a lightweight tibial link concept is translated into a (CAD) model, as illustrated in Figure 4.13. Given an estimated total mass of the robot, $m_{tot} = 10[kg]$, and a total length of $L_{tot} = 0.55[m]$, the non-dimensional tibial design parameters are computed using the following equation (Equation 4.20).

$$\begin{aligned} L_T &= L_T^* \cdot L_{tot} = 0.3909[m] \\ m_T &= 0.312[kg] \Rightarrow \\ m_T^* &= m_T/m_{tot} = 0.03116 \\ l_T &= 0.1872[m] \Rightarrow \\ l_T^* &= l_T/L_T = 0.4788 \\ I_T &= 0.007108[Kg \cdot m^2] \Rightarrow \\ I_T^* &= I_T/(m_T \cdot L_T^2) = 0.1493 \end{aligned} \tag{4.20}$$

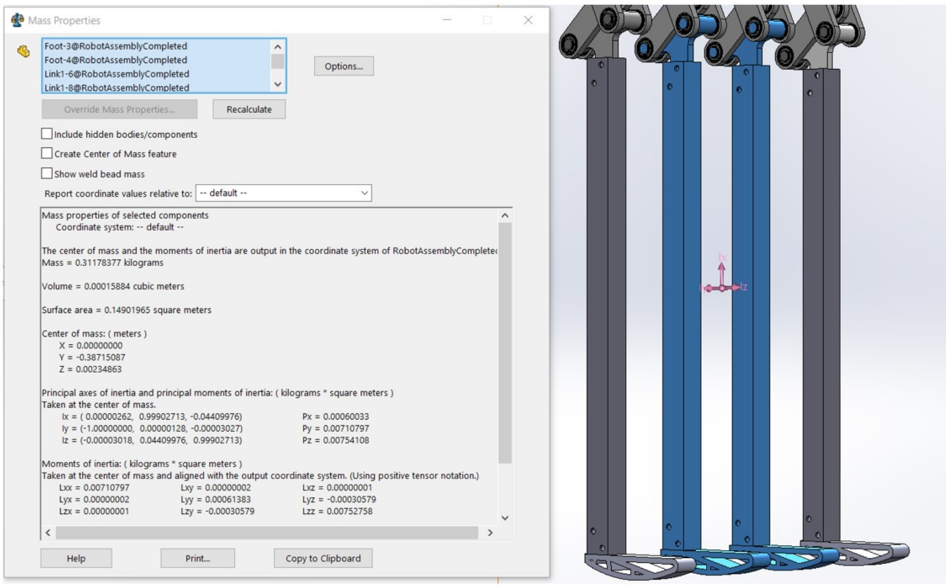

Figure 4.13: Tibial link design. The design is composed of, an aluminum part that connects the knee kinematic linkage with the tibial link, an off-the-shell rectangle carbon fiber tube, and an abs plastic foot limb.

The non-dimensional model parameters, which are computed using Equation 4.20, remain constant throughout the second optimization phase. The optimization process now focuses on the parameters lx_T^*, m_F^*, l_F^*, and I_F^*. The objective function weights remain unchanged. Similar to the first optimization, the gradient-based optimization is executed for a total of 20 iteration steps. The progression of the optimization can be visualized in Figure 4.14, while a comparison of the optimization parameters before and after the process is presented in Table 4.5. Additionally, for reference, key performance metrics are provided in Table 4.6 both before and after the optimization, as in the previous section.

b	Before the optimization	After the optimization	Difference
lx_T^*	0.0369	0.0621	+0.0252
m_F^*	0.0542	0.0509	-0.0033
l_F^*	0.2670	0.2728	+0.0057
I_F^*	0.1350	0.1442	+0.0092

Table 4.5: Optimization parameters before and after the second optimization

Metric	Before the optimization	After the optimization	Difference
$\bar{\lambda}_{max}$	0.6737	0.2202	-0.4535
$d_{min}[m]$	0.0021	0.0038	+0.0017

Table 4.6: Metrics of interest before and after the second optimization

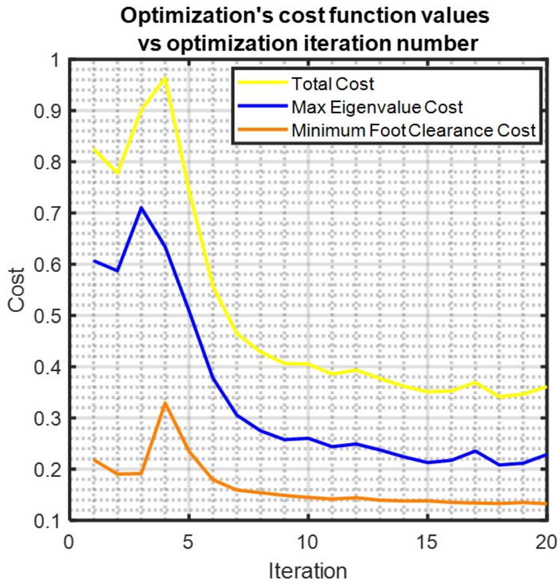

Figure 4.14: Semi-constrained optimization. The second phase of the optimization procedure. Initial a high non-linearity in the maximum eigenvalues leads to a spike in the total cost function. Despite that, the method again manages to converge in less the 20 iterations.

4.4.3 Third constrained optimization

After the second optimization, valuable insights are gained regarding the optimal design of the femoral link. This information contributes to the development of a comprehensive design, where the femoral link plays a pivotal role, serving as the housing for the knee actuator and knee motion transfer mechanisms and is depicted in Figure 4.15. The design used as an example in Subsection 4.3.3 serves as the initial CAD model for the third and final optimization phase. In this iteration, the optimization process is subject to constraints imposed by the CAD model. Furthermore, a specific target total mass, denoted as $m_{target} = 8,$ Kg, is established as an additional constraint.

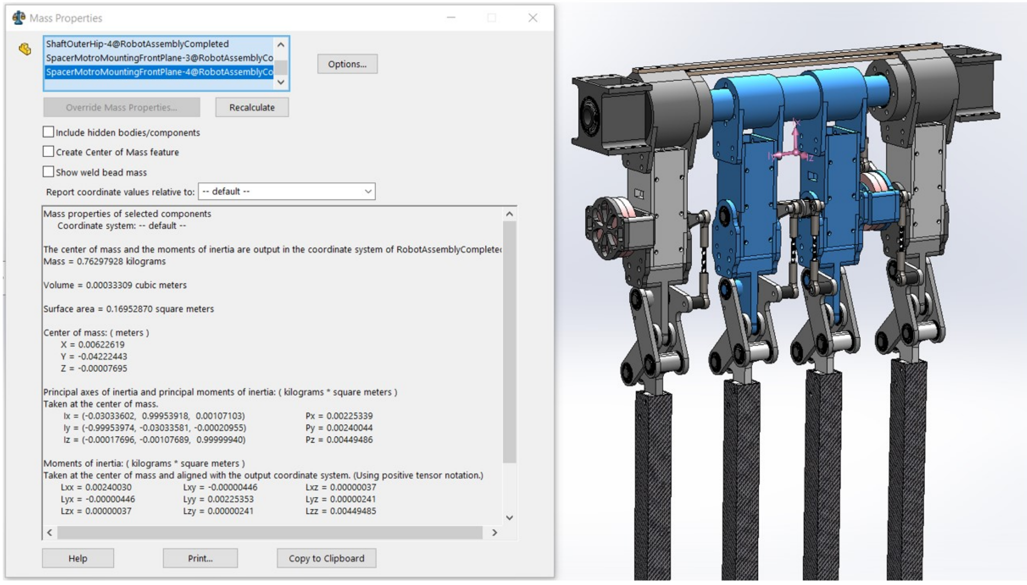

Figure 4.15: Femoral link design. The design is composed of, an aluminum assembly that connects the hip joint with the femoral link, an abs plastic 3D printed beam that also acts as casing for the motor and sensor cables, and an an aluminum structure that connects the knee kinematic linkage with the femoral link and additionally acts as the knee motor mounting

Before commencing the third optimization phase, it is essential to conduct a sensitivity analysis to determine the appropriate optimization weights. This analysis is detailed in Table 4.7. After consideration of the sensitivity evaluation results, the following weights were selected: $w_{\bar{\lambda}} = 0.5$, $w_{d_{min}} = 5e-4$, $w_{construction} = 0.1$, and $w_{mass} = 5e-2$.

The final optimization encompasses all inertial design parameters, which include L^*_F, l^*F, l^*T, lx^*_T, m^*F, m^*T, I^*_F, and I^*_T.

The gradient-based optimization process extended to 50 iterations during this phase and effectively reduced the total construction weight and the deviation from the CAD construction characteristics at the cost of the maximum eigenvalue, as depicted in Figure 4.16. A comparison of the optimization parameters before and after this phase is presented in Table 4.8. Furthermore, Table 4.9 offers insight into the optimization metrics of interest both before and after this final optimization.

b	$\frac{\delta \nabla F_{\bar{\lambda}}}{\delta b}$	$\frac{\delta \nabla F_{d_{min}}}{\delta b}$	$\frac{\delta \nabla F_{construction}}{\delta b}$	$\frac{\delta \nabla F_{mass}}{\delta b}$
L_F^*	-4.4895	0.0419 $\cdot 1e-4$	-1.1603	22.5264
l_F^*	6.5055	-0.0714$\cdot 1e-4$	0	0
l_T^*	2.2880	0.1035$\cdot 1e-4$	0	0
lx_T^*	11.4082	-0.0286$\cdot 1e-4$	0.4233	0
m_F^*	9.9838	-0.5404$\cdot 1e-4$	-6.2709	-736.9261
m_T^*	6.2578	1.0363$\cdot 1e-4$	10.5779	-736.9261
I_F^*	-3.0292	-0.0500$\cdot 1e-4$	24.3383	0
I_T^*	-4.5852	-0.2865$\cdot 1e-4$	0	0

Table 4.7: Third optimization sensitivities

b	**Before the optimization**	**After the optimization**	**Difference**
L_F^*	0.2893	0.2795	-0.0098
l_F^*	0.2728	0.2731	+0.0003
l_T^*	0.4788	0.4778	-0.0010
lx_T^*	0.0621	0.0586	-0.0034
m_F^*	0.0509	0.0800	+0.0290
m_T^*	0.0312	0.0334	+0.0023
I_F^*	0.1442	0.1382	-0.0059
I_T^*	0.1493	0.1553	+0.0060

Table 4.8: Optimization parameters before and after the third optimization

Metric	**Before the optimization**	**After the optimization**	**Difference**
$\bar{\lambda}_{max}$	0.2413	0.2560	+0.0147
$d_{min}[m]$	0.0038	0.0053	+0.0015
$F_{construction}$	0.5440	0.3387	-0.2053
$m_{tot}[Kg]$	11.9536	8.6212	-3.3324

Table 4.9: Metrics of interest before and after the third optimization

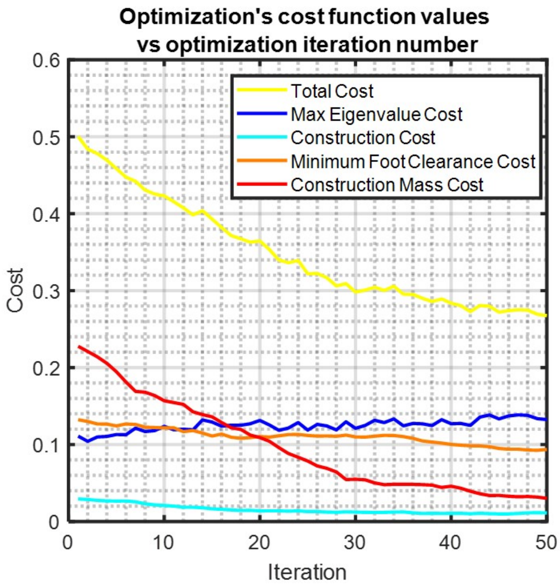

Figure 4.16: Constrained optimization. The third phase of the optimization procedure. The optimization convergence is more demanding so 50 optimization iterations were selected. It's important to note that the cost associated with the construction deviation from the CAD model, minimum foot clearance, and total mass are decreasing, while the cost related to the maximum eigenvalue is increasing. This trade-off reflects the practical constraints and indicates that the design optimization procedure has pushed the model to its performance limits.

4.5 Final design

The final optimization step has been successfully completed, and the last phase of the procedure involved generating a final CAD design that closely aligns with the design suggested by the Matlab optimization. After making some design adjustments, the CAD model was finalized. The discrepancies between this CAD model and the optimized model are detailed in Tables 4.10 and 4.11. You can also view the final CAD model in Figure 4.17.

b	Optimization Results	Inner CAD foot	Difference
$L_F[m]$	0.1537	0.1537	0
$L_T[m]$	0.3963	0.3963	0
$l_F[m]$	0.0420	0.0451	0.0032
$l_T[m]$	0.1893	0.1896	0.0003
$lx_T[m]$	0.0232	0.0234	0.0002
$m_F[Kg]$	0.6893	0.7063	0.0170
$m_T[Kg]$	0.2883	0.2887	0.0004
$I_F[Kg \cdot m^2]$	0.0023	0.0024	0.0001
$I_T[Kg \cdot m^2]$	0.0070	0.0074	0.0004

Table 4.10: Inner foot CAD model inertial parameters vs Optimized model inertial parameters. (The parameters are dimensional)

b	Optimization Results	Inner CAD foot	Difference
$L_F[m]$	0.1537	0.1537	0
$L_T[m]$	0.3963	0.3963	0
$l_F[m]$	0.0420	0.0438	0.0019
$l_T[m]$	0.1893	0.1896	0.0003
$lx_T[m]$	0.0232	0.0234	0.0002
$m_F[Kg]$	0.6893	0.7059	0.0166
$m_T[Kg]$	0.2883	0.2887	0.0004
$I_F[Kg \cdot m^2]$	0.0023	0.0027	0.0004
$I_T[Kg \cdot m^2]$	0.0070	0.0074	0.0004

Table 4.11: Outer foot CAD model inertial parameters vs Optimized model inertial parameters. (The parameters are dimensional)

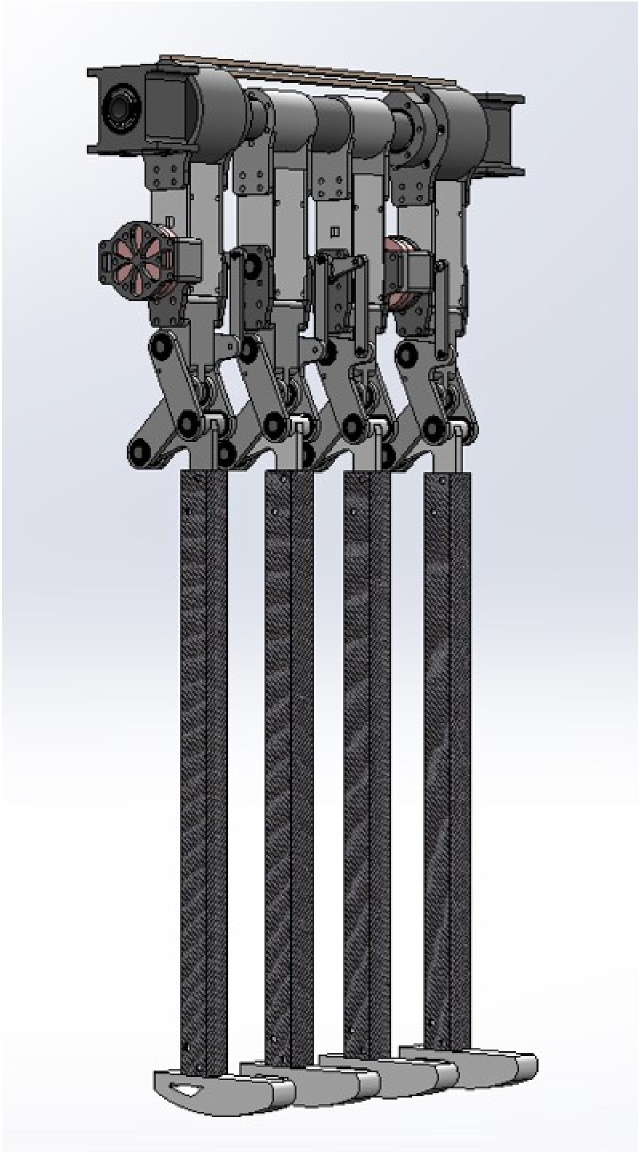

Figure 4.17: The CAD model has been designed to closely match its inertial parameters with those of the optimized model, ensuring a high degree of similarity between the two.

5 Active Robot

To evaluate the robot's gait when being actuated initially a Matlab simulation where conducted with the augmented model. The augmented active robot consists of the same parameters with an additional hip of which the center of mass is located out of the hip axes.

5.1 Cad model

The design principle of the robot is to maintain identical inertial parameters for both the passive and active robot models. This approach not only reduces the overall cost of the experimental platform but also allows for the execution of both passive and active robot experiments on the same platform. To achieve that an active robot model is constructed keeping all the parameters the same except the location of the hip's center of mass which is shifted away from the hip axis to l_{CW}

distance. Comparing the results of passive and active gaits becomes feasible, and importantly, the optimization algorithm remains consistent (see Figure 5.1).

The fundamental design principle of the robot is to maintain identical inertial parameters for both the passive and active robot models. This not only reduces the overall cost of the experimental platform but also enables the execution of both passive and active robot experiments on the same platform. To achieve this, an active robot model is constructed, keeping all parameters the same except for the location of the hip's center of mass, which is shifted away from the hip axis to a distance of l_{CW} (5.1).

This design choice facilitates the comparison of results between passive and active gaits. Importantly, the optimization algorithm remains consistent.

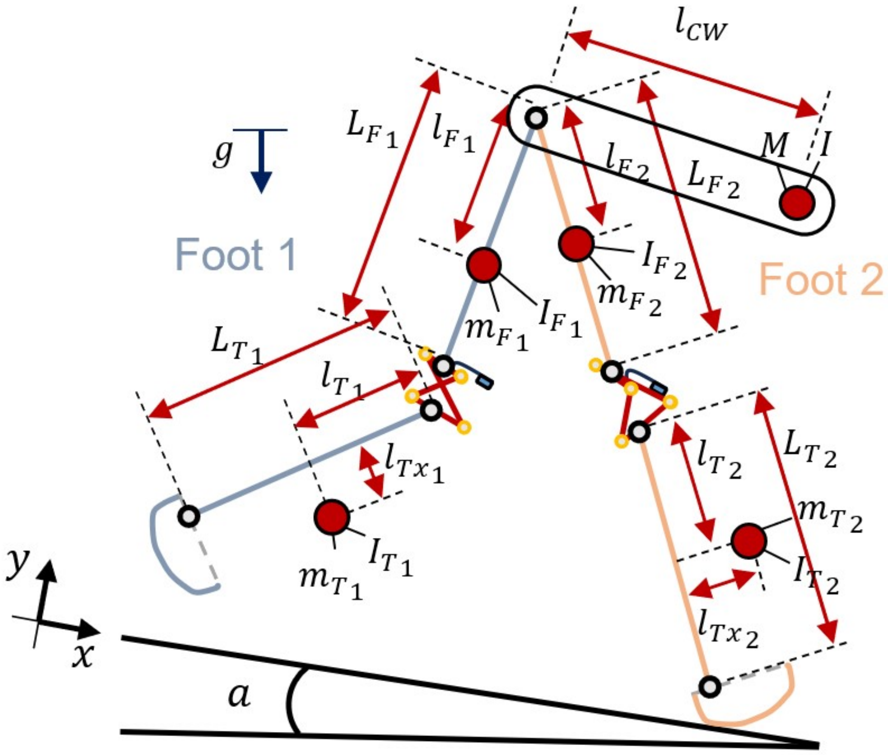

Figure 5.1: Active robot model parameters

To achieve this objective, a hip with counterweights is introduced. The location of the counterweights influences the center of mass distance from the femoral axle (see Figure 5.2). In the passive configuration, the robot's center of mass coincides with the femoral axle. In contrast, the active configuration positions the center of mass away from the axle, creating a lever. This lever facilitates torque production between the femoral and hip links without the link's overturn.

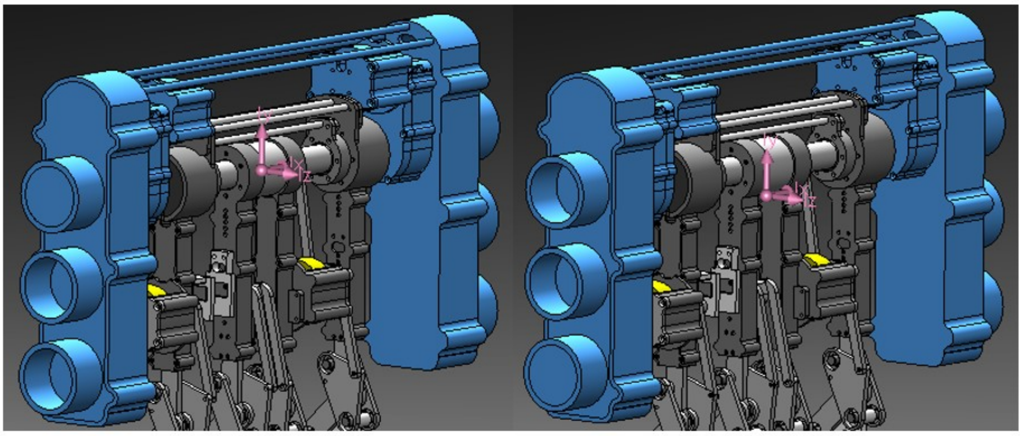

Figure 5.2: Femoral joint torque time-series. Almost constant torque is needed.

5.2 Simulation

5.2.1 Matlab active robot model

To reassure the active robot's operation initial simulations are conducted in Matlab. The parameters of the active robot as well as the initial conditions calculated from the passive model are inserted. The control scheme conducted by Fotis Valouxis is used. A comparison between the passive and active robot's gait is presented in Figure 5.3

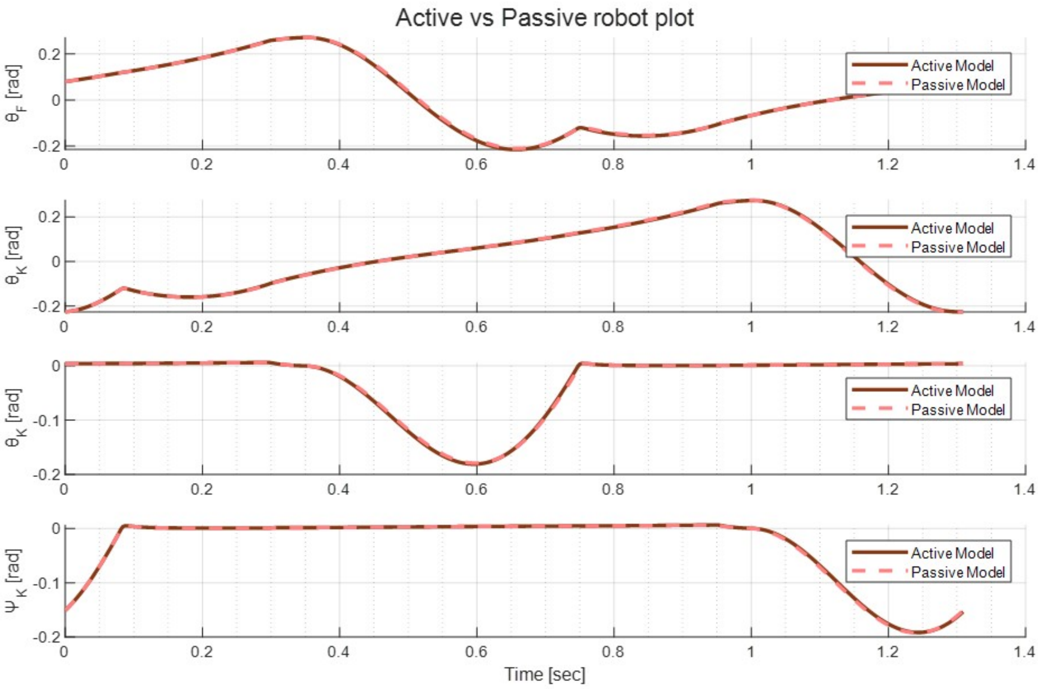

Figure 5.3: Comparison between the joint trajectory of the passive robot walking on a slope of -0.6 [deg] and the active robot walking on the flat with a -0.6 [deg] slope gravity compensation. It is noted that the relative difference between the trajectories is very small and those differences can be attributed to the Matlab solvers used.

The analysis extends to assessing whether the robot can maintain stable walking with and without knee actuation in non-zero slopes. The robot's gait is examined on multiple slopes under two scenarios: full joint actuation (Full Actuation System) and femoral joint actuation only (Quasi Actuation System).

In the fully actuated system, the robot can walk until its hip is unable to produce the required counter torque. This limitation occurs at a maximum positive slope of $0.9[deg]$ and a minimum negative slope of $-2.1[deg]$. For the quasi-actuated system, it is observed that the tibial link swing is not dramatically affected by changes in slope (see Figure 5.4). In positive slopes, the knee cap maintains knee lock, allowing the robot to operate until the maximum slope of $0.9[deg]$. In negative slopes, the stance knee joint tends to fold until reaching a slope of $-1.1[deg]$ where it finally collapses. (see Figure 5.5).

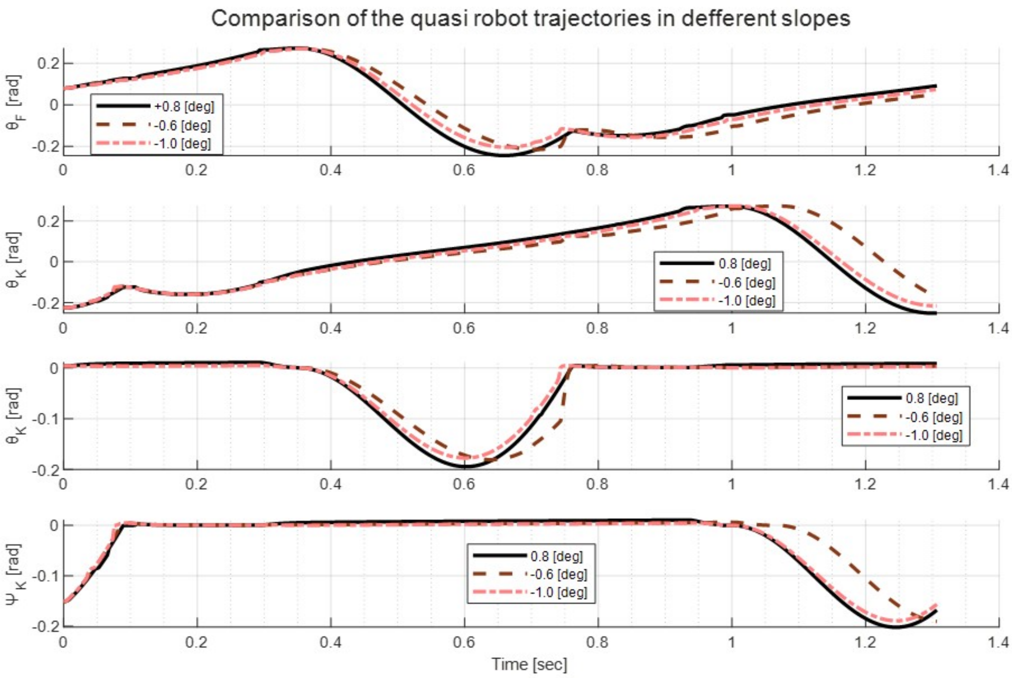

Figure 5.4: Trajectories of the robot without knee actuation for different slopes. It is noted that the trajectory at the slope $-0.6[ded]$ coincides with those of the fully actuated robot, as $-0.6[deg]$ gravity compensation is implemented.

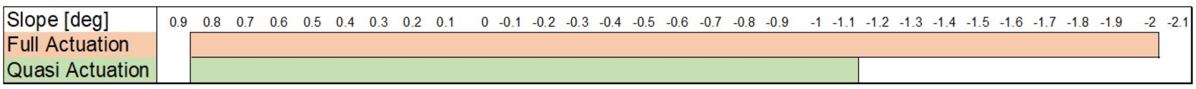

Figure 5.5: Operation capability of the robot at different slopes. The full-actuated robot has actuation on both the femoral and knee joints. The quasi-actuated robot has actuation only on femoral joints.

5.2.2 Adams active robot model

Utilizing the model parameters and the robot's position, a gravity compensation control can be applied to Adams for validation. This ensures the effectiveness of the control even in a more detailed simulation environment. To achieve this, a Simulink-Adams co-simulation is created, where Simulink provides a torque command at each Adams time step. The Adams model is incorporated as a block in the Simulink environment (see Figure 5.6). The torque control is implemented by reading the Adams simulation's model state at each time step and the inertial parameters of the CAD model. A Matlab's torque compensation algorithm calculates torque commands, which are then fed to the Simulink model. Additionally, the algorithm estimates which foot is in contact with the ground.

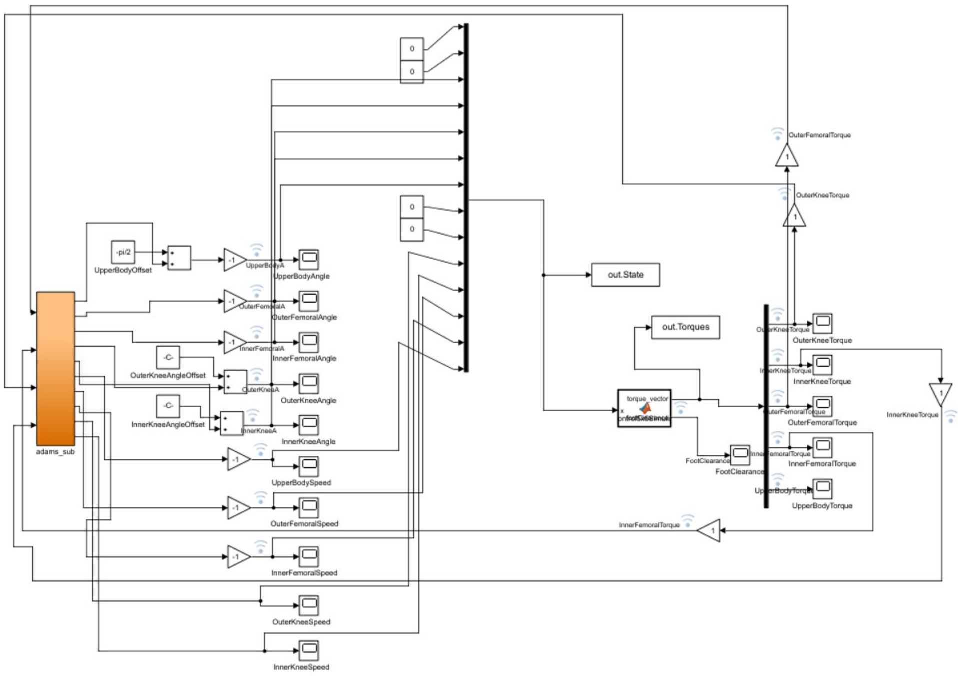

Figure 5.6: Adams-Matlab cosimulation model.

The Adams robot model demonstrates effective walking when the gravity compensation control designed in Matlab is applied. It is crucial, however, to evaluate the disparities between the gait produced in the Matlab environment and the gait produced in the Adams environment. This comparison aims to characterize the differences between the results of the two environments and assess their significance (See Figure: 5.7).

The gait patterns in the two models exhibit a similar form. However, it's noticeable that in the Adams environment, a smaller gait period and a reduced swing angle span of the Femoral link are observed. This suggests a lower energy content fixed point for the simulation in the Adams environment. Several factors, outside the scope of this study, could contribute to this observation. Possibilities include higher energy dissipation during ground contact, energy loss during the foot's interaction with the ground, or a small yaw angle during the robot's gait. Despite these differences, the results are considered acceptable for the continuation of the study.

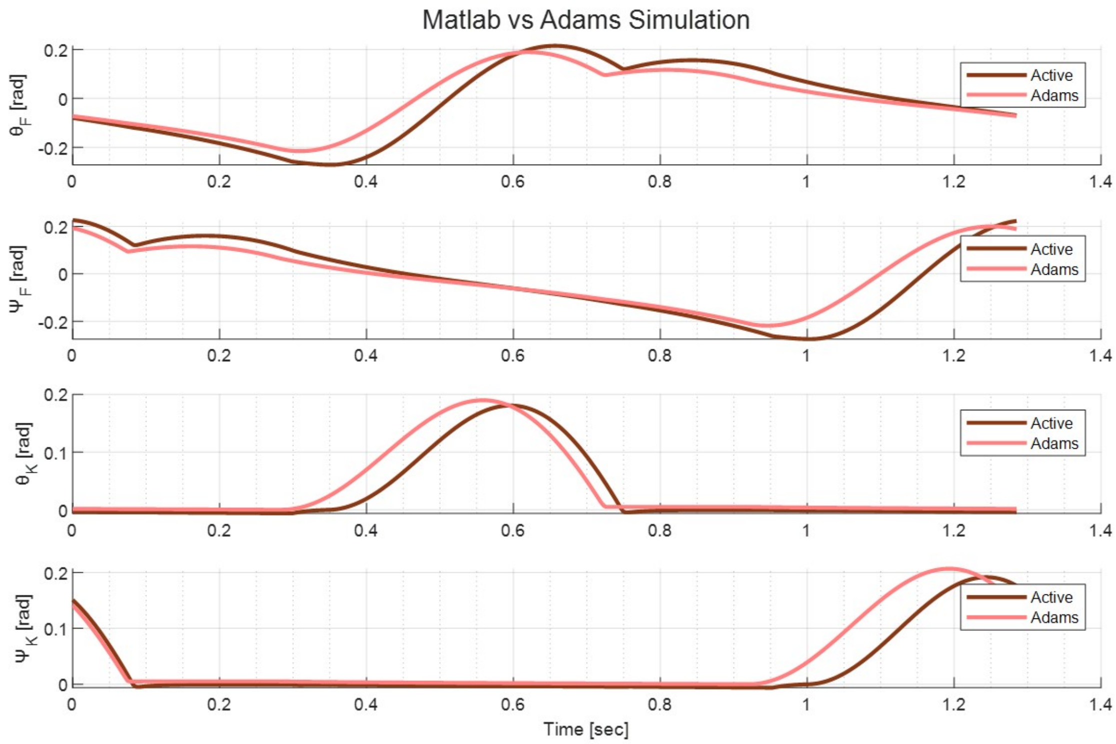

Figure 5.7: Comparison of Matlab and Adams state time-series during a complete step. It is noted to avoid misconceptions that both models have reached their fixed point at the time the measurements are taken.

5.2.3 Simulation in multiple operating conditions

Given the control scheme in an operation state, simulations for different slopes are conducted to calculate the different slope scenarios' torque demands. The hip's initial condition depends on the torque needs.

5.3 Speed Reduction Systems

A critical aspect of active robot design is the actuation system. The robot operates under torque control, leveraging its passive dynamics. The specific application prioritizes low reflected inertia and high back-drivability, aiming to closely align the inertial characteristics of the active robot with those of the passive counterpart. Consequently, a proprioceptive actuation system must be designed, employing high-torque motors with low-reduction systems for both the femoral and knee joints.

5.3.1 Femoral Joint Reduction System

The femoral actuation system is designed to be lightweight with a low reduction ratio, aiming for small reflected inertia and high torque transparency during the robot's operation in active mode. The torque-speed demand of the femoral joint is depicted in Figure 5.8. The highest torque-power demand occurs when the robot is controlled with a $-0.6[deg]$ compensation ascending a slope of $0.8[deg]$. In Figure 5.9, the time-series of the torque demand for this scenario is presented.

The torque time series reveals a constant torque demand, indicating low bandwidth demands for the reduction system. Consequently, an in-house pulley reduction system design is considered the most cost-effective and customizable solution.

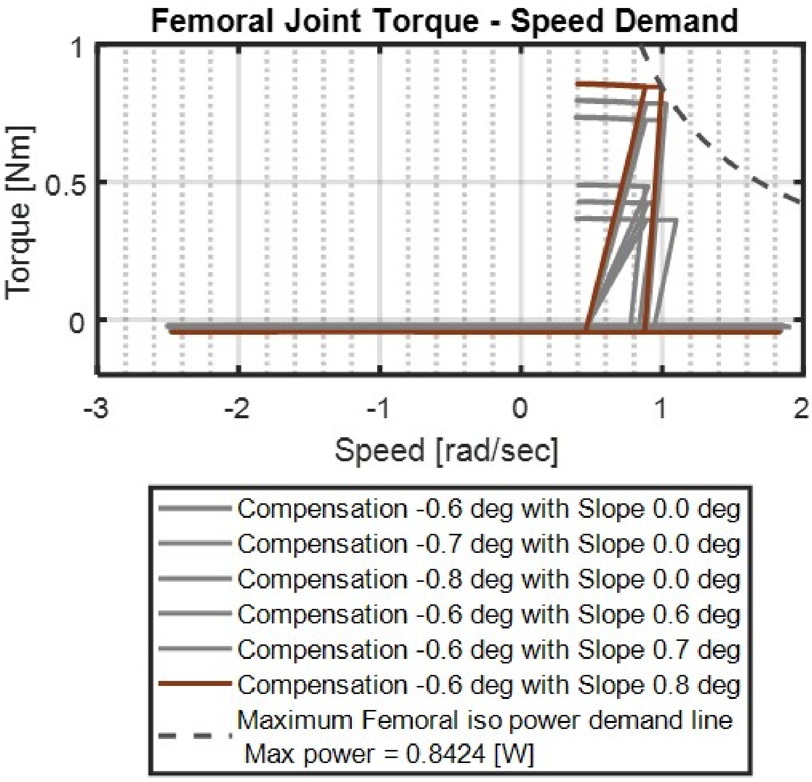

Figure 5.8: Femoral joint torque - speed demand.

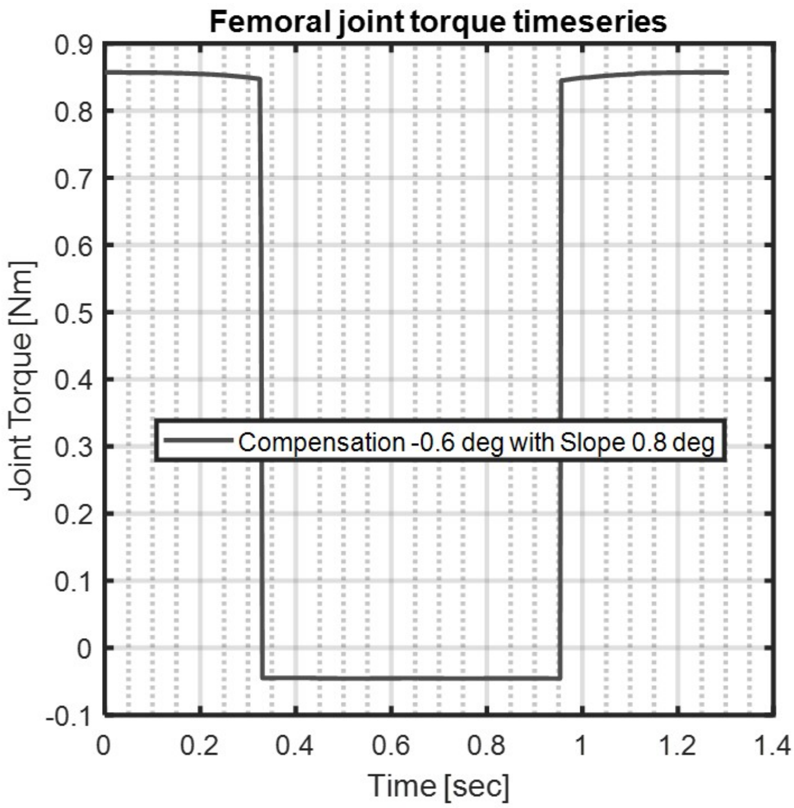

Figure 5.9: Femoral joint torque demand time series.

There is a need to achieve a compact pulley design (see Figure 5.10. The system is composed of two pulleys the high teeth number pulley will be mounted to the main femoral shaft while the low teeth number pulley is mounted to the pulley housing shaft. The housing shaft is connected to the motor which is mounted on the housing. The location of the low teeth number pulley is determined to be such that facilitates the pulley belt size availability from local stores. From the casing side across the motor mounting side, the hip is mounted. The pulley tension is achieved by a pulley idler mounted on a shaft sub-construction that can be linearly driven through the pulley's casings' internal slots by tightening a set screw on the pulley housing. The housing that plays the structural role is designed to ease the decoupling of the belt during the motor setup and calibration procedure. To avoid the direct exposure of the system's internal components to the environment a plastic cover is added to the pulley housing.

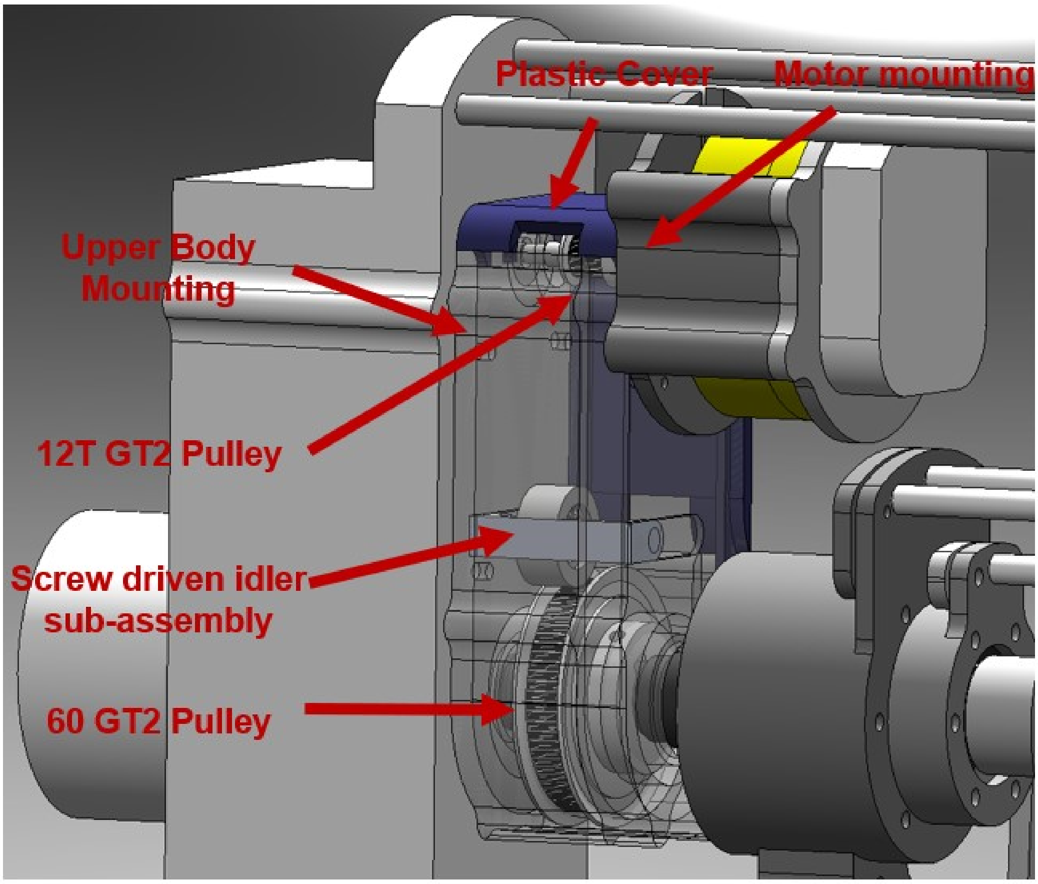

Figure 5.10: Pulley system description

Given the standard pulleys available the low and high teeth number pulleys are selected to maximize the reduction achieved. Finally, the low teeth side pulley is selected to be of 12 teeth while the high teeth pulley is selected to be of 60 teeth. The overall reduction value is 5.

5.3.2 Knee Joint Reduction System

For the knee joint (see Figure 2.1), the analysis indicates a demand for high torques at low speeds and vice versa, with the total joint power remaining relatively small throughout the operational cycle (see Figure 5.11). Consequently, an efficient solution involves implementing a speed reduction system with a high reduction ratio for angles requiring high torque and a lower reduction ratio for angles demanding high speed. Notably, the system must adhere to strict constraints of compactness and lightweight design, given the motor's location. To meet these criteria, a four-bar mechanism is chosen, as it satisfies all specified requirements if designed systematically. It is noted that again the most demanding gait scenario is that of compensation of $-0.6[deg]$ with the robot ascending a slope of $0.8[deg]$. The time series of the knee joint torque demands for this scenario is presented in Figure 5.12.

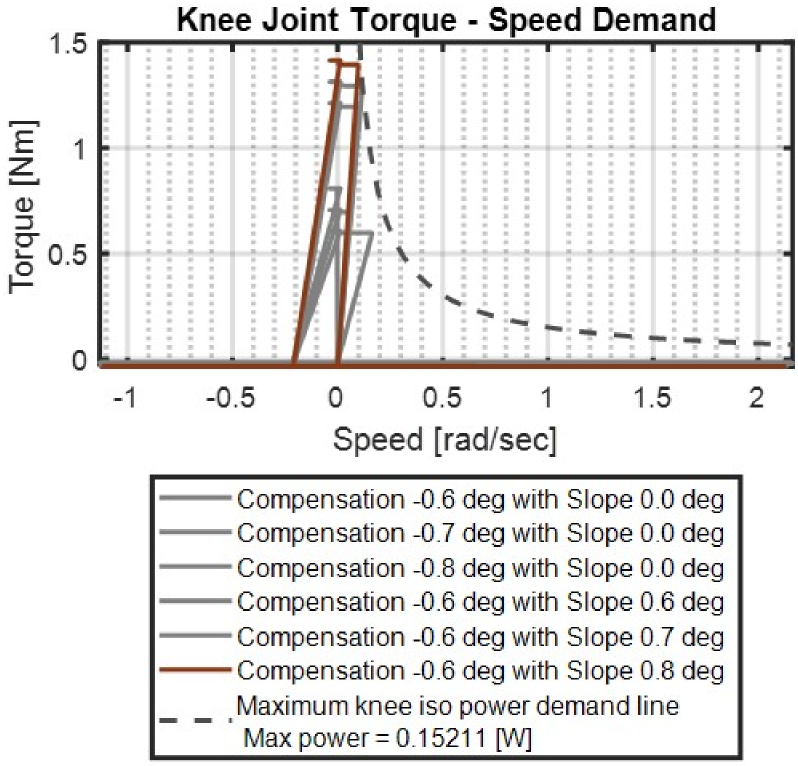

Figure 5.11: Knee joint speed and torque requirement for different robot's operation conditions. Notable the joint tends to operate at relatively high torques during periods of reduced speeds and conversely at high speeds when subjected to low torque demands.

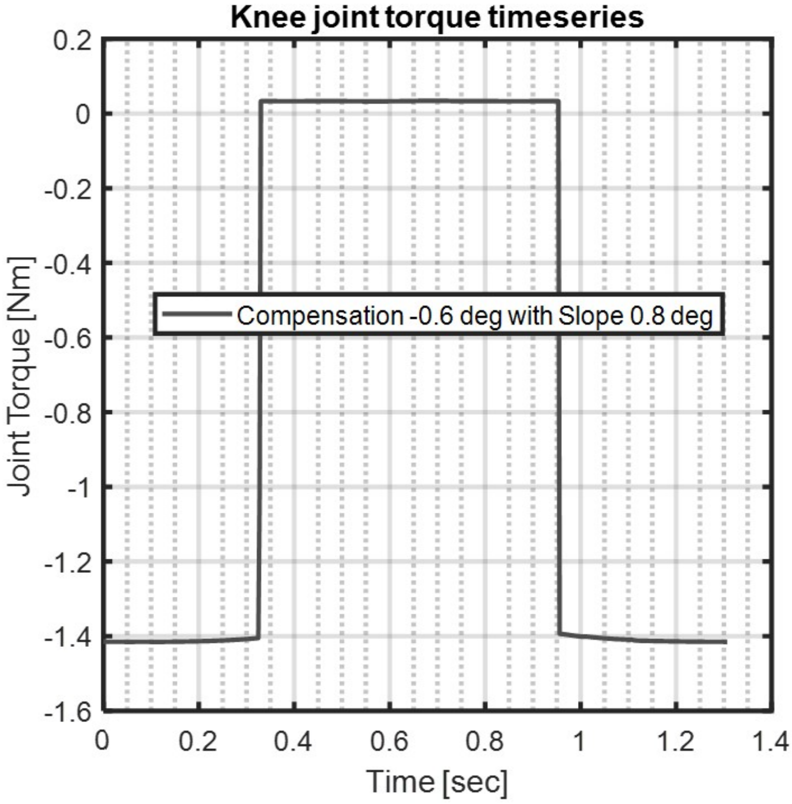

Figure 5.12: Knee joint torque demand time series.

The process of finding a four-bar mechanism suitable for the specific application is not a straightforward procedure and the mechanism geometry and its mounting to the robot must be modeled in a structured way that will enable the optimum mechanism selection. According to figure 5.13, The mechanism geometry is described by four parameters the input link a, the output link b, the floating link that connects the input and the output link f, and the ground link g. The mounting of the link can be described by the offset angle θ_{offset}.

For the rest of the analysis, it will be useful to additionally define the non-dimensional mechanism configuration (see Equation 5.1).

$$\begin{aligned} a^* &= a/g \\ b^* &= b/g \\ f^* &= f/g \\ \theta^*_{offset} &= (\theta_{offset} - \theta^{a^*,b^*,f^*}_{min})/(\theta^{a^*,b^*,f^*}_{max} - \theta^{a^*,b^*,f^*}_{min}) \end{aligned} \tag{5.1}$$

Where $\theta^{a^*,b^*,f^*}_{min}$ is the initial angle of the mechanisms operation span and $\theta^{a^*,b^*,f^*}_{max}$ is the final angle of the mechanisms span.

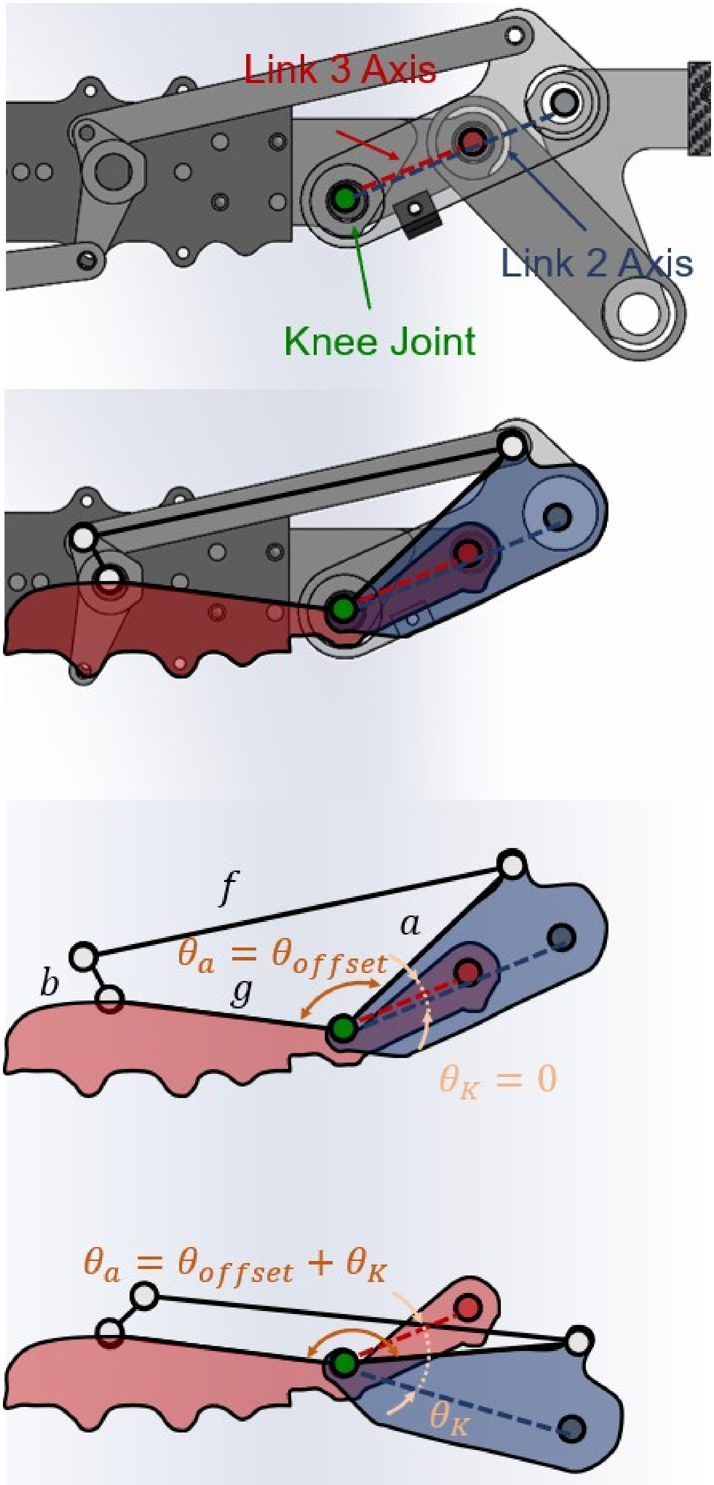

Figure 5.13: Parameterization of the four-bar reduction mechanism according to its geometry and its mounting on the robot

The mechanism has to operate in an angle span that can produce the output angles needed without reaching its geometrical limits. Also, the mechanism has to be backdrivable from both the input and output side. This means that the operation span of the mechanism has to be away from singularities both from the input and the output side. The possible singular configurations of a four-bar mechanism are four. The first two are when the link b is collinear to link f with relative angle 0^o or 180^o ($\theta^{b.exp}$, $\theta^{b.fold}$) and the remaining two are when the link b is collinear to link f again with relative angle 0^o or 180^o ($\theta^{a.exp}$, $\theta^{a.fold}$). See Figure 5.14. The limit angles can be calculated by simple trigonometry (see equation 5.2).

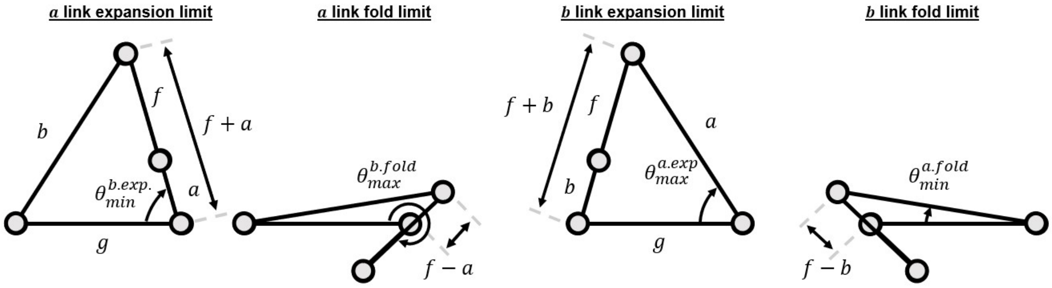

Figure 5.14: Four bar operation possible limiting angles. The four-bar mechanism operation is limited to the presented angles if they exist in order to avoid singularities in the mechanism operation.

$$
\begin{aligned}
\theta^{b.exp} &= \arccos\frac{(f+a)^2+g^2-b^2}{2\cdot(f+a)\cdot g} \\
\theta^{b.fold} &= \arccos\frac{(f-a)^2+g^2-b^2}{2\cdot(f-a)\cdot g}+\pi \\
\theta^{a.exp} &= \arccos\frac{(f+b)^2+g^2-a^2}{2\cdot(f+b)\cdot g} \\
\theta^{a.fold} &= \arccos\frac{(f-b)^2+g^2-a^2}{2\cdot(f-b)\cdot g}
\end{aligned}
\tag{5.2}
$$

Depending on the non-dimensional parameters a^*, b^*, f^* the limiting angle type varies. To ease the categorization process of the different cases a linkage parameter transformation ($[a^*, b^*, f^*] \rightarrow [T_1, T_2, T_3]$) is executed (see equation 5.3). The sign of those parameters (T_1, $T2$, and T_3), given that the mechanism configurations of interest shape a convex area when their links are not intersected, can predict the initial and final limit angle ($\theta^{a^*,b^*,f^*}_{min}$, $\theta^{a^*,b^*,f^*}_{max}$) type (see Figure 5.15).

$$
\begin{aligned}
T_1 &= 1+f^*-(a^*+b^*) \\
T_2 &= 1+b^*-(a^*+f^*) \\
T_3 &= 1+a^*-(b^*+f^*)
\end{aligned}
\tag{5.3}
$$

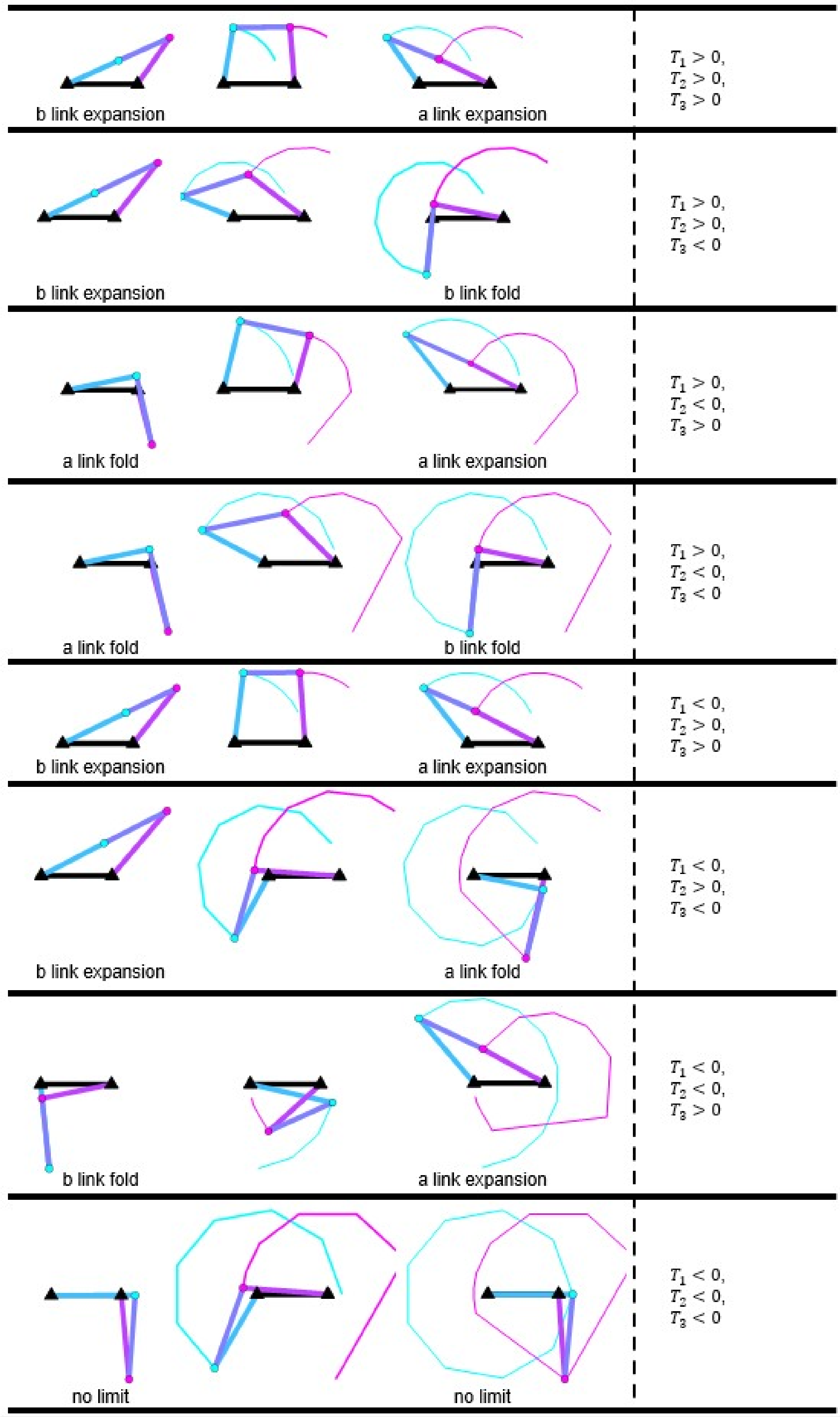

Figure 5.15: Limit angle types based on the T_1, $T2$, and T_3 parameters

To determine the most suitable link for the specific application an extended search optimization for the non-dimensional four-bar link parameters a^*, b^*, f^* and θ^*_{offset} is conducted. Initially, reasonable spans of the non-dimensional parameters are set: $a^* = (0.2, 0.5)$, $b^* = (0.15, 1)$, $f^* = (0.7, 1.6)$, $\theta^*_{offset} = (0, 1)$.

During the extensive search procedure, each one of the mechanism configurations is generated. The input side is loaded based on the knee link's torque and speed demands during a zero slope with $-0.6[deg]$ gravity compensation gait cycle. The objective is to minimize the maximum torque required from the mechanism output (motor) side. Two specifications are enforced: the mechanism input side must maintain at least a 30 [deg] operational margin from the trajectory limit angle, and throughout the trajectory, the mechanism must generate speed reductions between $(0.1, 10)$ to ensure sufficient distance from singularity limits. In case of at least one restriction violation, the mechanism is characterized as invalid.

The optimum mechanism is the mechanism with the parameters: $a^*_{opt} = 0.5$, $b^*_{opt} = 0.15$, $f^*_{opt} = 1.2789$ and $\theta^*_{offset,opt} = 0.0201$. The resulting value of link a^* and b^* is straightforward as the higher $input/output$ link length ratio is the higher the achievable reduction is. For the floating link length f^* and the offset angle ratio and the θ^*_{offset} the following visualization indicates the optimum point (see Figure 5.16). To validate the reduction achieved during the knee operation the mechanism is implemented to the knee joint trajectory and the reduction achieved is recorded throughout a complete gait (see Figure 5.17).

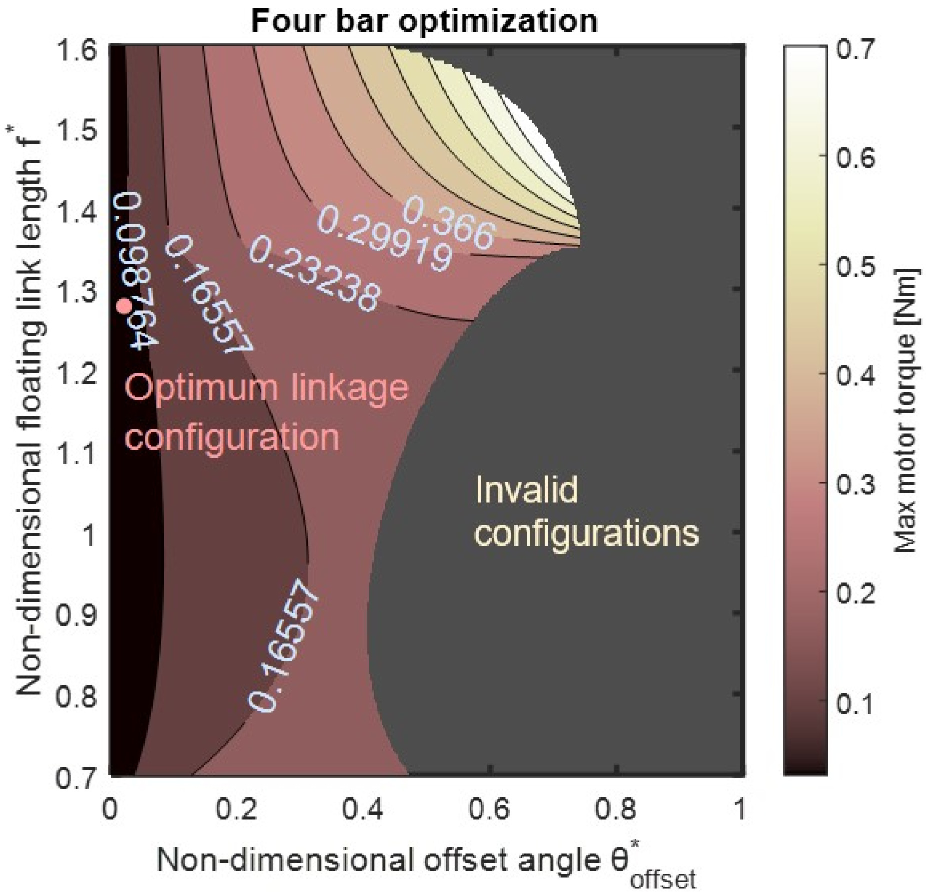

Figure 5.16: Maximum input/motor side torque map relative to the non-dimensional offset angle θ^*_{offset} and the non-dimensional floating link length f^*. For high θ^*_{offset}, the mechanism can not achieve the minimum operational margin needed, so it is considered invalid.

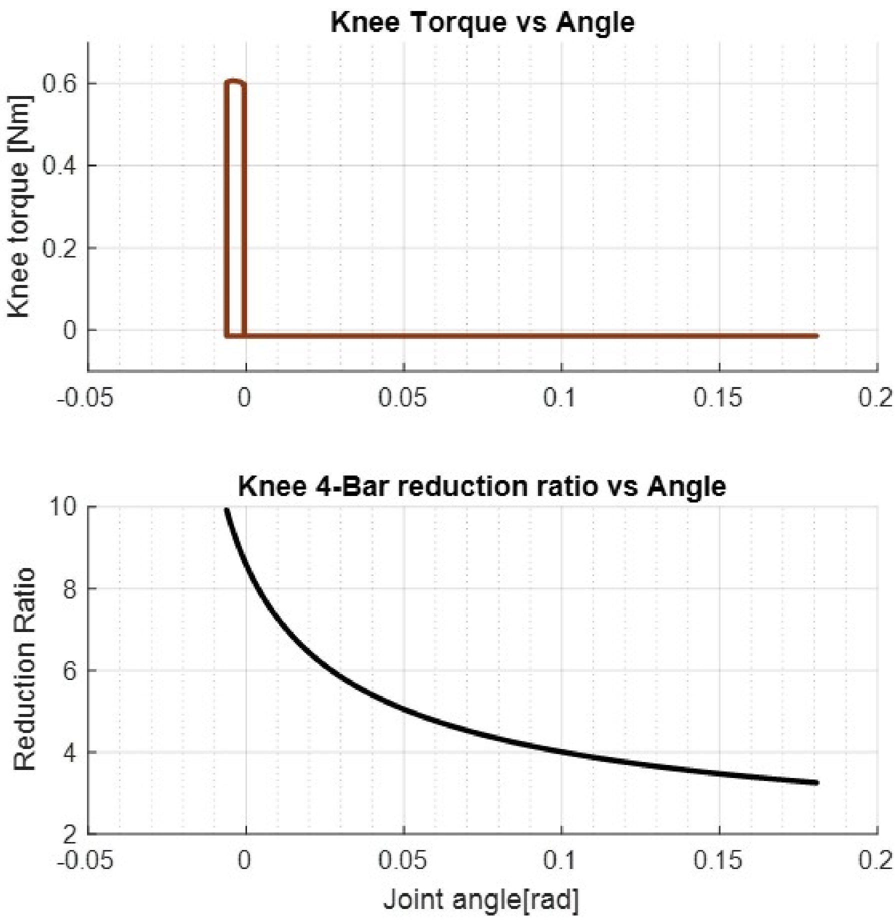

Figure 5.17: Reduction ration of the four-bar mechanism when subjected to the joint trajectory. It can be observed that a high reduction ratio is achieved at angles where torque demands are high. The four-bar optimization procedure can be considered successful.

5.4 Motor

As highlighted in Section 5.3 introduction, the specific requirements of the application necessitate the use of high-torque motors to compensate for the low reduction systems. Moreover, torque controllability is a critical factor. These specifications lead to the selection of permanent magnet DC motors. Within this category, two options exist: brushed and brushless DC motors.

Brushless DC motors, devoid of mechanical brushes, offer higher robustness. Their electronic commutation eliminates wear due to friction and eliminates sparking phenomena. Furthermore, sophisticated commutation techniques can be employed for enhanced performance. The absence of mechanical brushes not only reduces weight but also allows for optimized spatial designs. However, it is worth noting that the drivers for Brushless DC motors are more complex and expensive.

On the other hand, brushed DC motors represent a more classic actuation solution with relatively reduced performance. They are characterized by simplicity, easy driveability, and the team's extensive experience.

5.4.1 Motor selection criteria

Several motor options in the market can achieve the torque-speed demands of the application. To select those that best feet to the kneed walker it is important to set some criteria that will affect the robot's performance.

The first main specification emerges from the robot's inertial characteristics strict specification. The motors are relatively heavy in comparison to the other robot's parts and this means that there is a need for a significantly low-mass motor. At the same time, it is important that the motor fulfills the joint's torque demands (it is noted that the motor speed demands are relatively low). This fact leads to the rated torque density motor metric (see equation 5.4). From two motors of the same torque, it is preferable to choose the one with the highest torque density as this will lead to total systems mass reduction and ease of the passive dynamic design process.

$$T^*_{rated} = \frac{T_{rated}}{m_{motor}} \tag{5.4}$$

The second main specification results from the fact that both joints operate at high torque with relatively low speeds (see Figure 5.11 and 5.8). According to the electric power consumption formula (see equation 5.5) this results in high ohmic losses relative to the mechanical power generated (see Figure ??). To reduce this phenomenon the zero-speed electric power to torque metric ($P^*_{el,speed0}$) has been conceived (see equation 5.6).

$$\begin{aligned} P_{el} &= I^2 \cdot R + |T_{motor} \cdot \omega_{motor}| \\ P_{el} &= T^2_{motor} \cdot \frac{R}{K_t^2} + |T_{motor} \cdot \omega_{motor}| \end{aligned} \tag{5.5}$$

If the motor speed is set equal to zero then the total electric power consumed is transformed into heat due to ohmic losses. The zero-speed electric power to torque metric arises.

$$\begin{aligned} P_{el,speed0} &= T^2_{motor} \cdot \frac{R}{K_t^2} \\ P^*_{el,speed0} &= \frac{R}{K_t^2} \end{aligned} \tag{5.6}$$

In addition, several supplementary criteria must be considered, including the added moment of inertia due to the motor's rotor, pricing, manufacturer reliability, accuracy of technical specifications, and dimensional considerations.

Based on the outlined criteria, along with other considerations, a table (see Table 5.18) is constructed to facilitate a direct comparison of different motor candidates. The T-Motors MN5008 Antigravity motor emerges as a strong option, combining high torque capabilities, a lightweight design, and low power consumption, particularly when operated at zero speeds. The manufacturer highlights its distinctive features, including arc-shaped magnets and high magneto-conductivity steel sheets, contributing to efficient operation. Furthermore, the logical multislot structure helps reduce motor cogging torque, ensuring smooth operation. From previous CSL lab works with T-Motors Antigravity models it is implied that the Back EMF of the motors is sinusoidal.

	Motors Comparison							
Motor	T-Motor GL40 KV70	iPower GM6208-150T	T-Motor GB54-2	T-Motor MN5008 Antigravity	Maxon EC 45 flat Ø42.8 mm, brushless, 60 W	Maxon DCX 35 L	Faulhaber Series 3863 ... CR	Porescap 35GLT2R82 326P
Manufacturer	CubeMars	iFlight	T-Motor	T-Motor	Maxon	Maxon	Faulhaber	Porescap
Type	BLDC Gimbal	BLDC Gimbal	BLDC Gimbal	BLDC Current	BLDC Current	Brushed	Brushed	Brushed
Size	Φ46.5*21.5	Φ69.5*24.0	Φ60.7*25.0	Φ55.6*32.0	Φ42.8*22.0	Φ35*70.0	Φ38*64.0	Φ38*67.2
Region	Poland	China	Spain	Spain	Switcherland	Switcherland	Switcherland	Switcherland
Price	74.14 [euro]	53.91[dolars]	74.9[euro]	89.99[euro]	157.89[euro]	350.00[euro]	491.95 [euro]	411.99 [euro]
Kv [rpm/V]	70	12	26	170	324	699	240	244
Kt [rpm/V]	0.136	0.25	0.367	0.056	0.030	0.029	0.040	0.039
Rated Current [A]	1.650	1.200	1.225	3.000	4.290	4.260	4.000	3.500
Rated Torque [Nm]	0.250	0.300	0.450	0.169	0.127	0.125	0.159	0.137
Resistance [Ω]	4.500	32.000	15.000	0.270	0.447	0.346	0.640	0.900
Motor Weight [g]	107.0	249.0	156.0	128.0	113.0	385.0	390.0	360.0
Rotor Inertia [gcm^2]	_	_	_	_	135	96.6	96.6	75
Power El. to Torque (0 Speed) [W/Nm^2]	241.8	512.0	111.2	85.6	513.6	403.0	404.0	588.7
Torque density [Nm/Kg]	2.336448598	1.204819277	2.884615385	1.316539051	1.119955752	0.324202597	0.408205128	0.380138889
Image								

Figure 5.18: Comparison of motor candidates.

5.4.2 Motor Validation

After selecting the motor candidate, it is crucial to implement it in the robot joint to validate its capability to support the robot's operation. During the robot's gait operation, whether in a zero-slope or ascending gait, the motor should be able to produce the torques and speed needed assuming a 22.2 Volts battery (see Figure 5.19). Additionally, the motor RMS current should not exceed the constant current limit (see Figure 5.20) to ensure thermal safety. For the motor MN5008, it is evident that the motor meets the specified requirements. Notably, both joints utilize the same motor, as the torque demands are close.

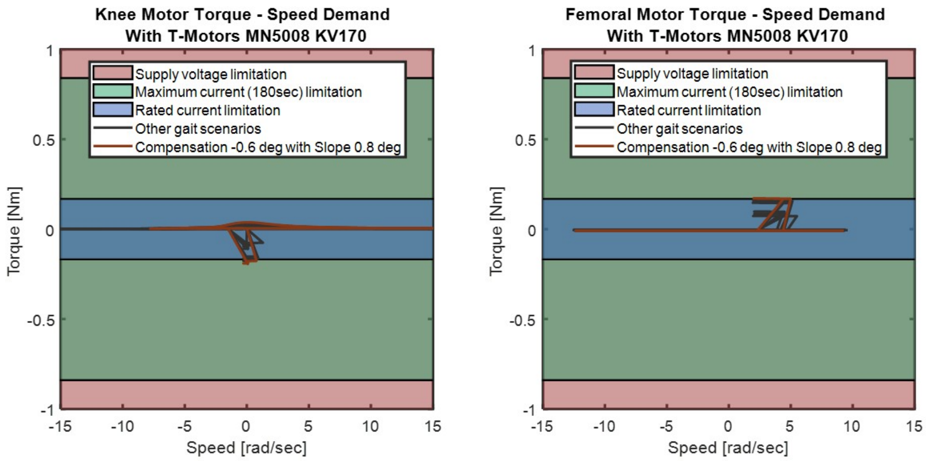

Figure 5.19: Motor speed torque map mounted on femoral joint and tibial joint.

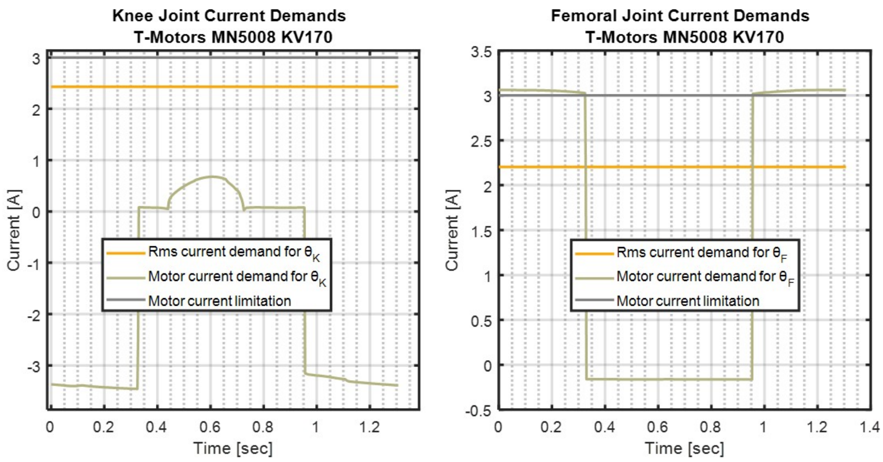

Figure 5.20: Motor current demands and current RMS demand value. It noted that the RMS value is within the constant current limit of the motor.

Figure 5.21 illustrates the robot's electric power consumption, notably higher than the mechanical power produced. Furthermore, the figure highlights the minimal mechanical power generated from the knee joint. In Section 5.2.1 it is noted that the knee actuation is possible to get disabled. This not only reduces electric power consumption but also lowers the overall cost of the robot.

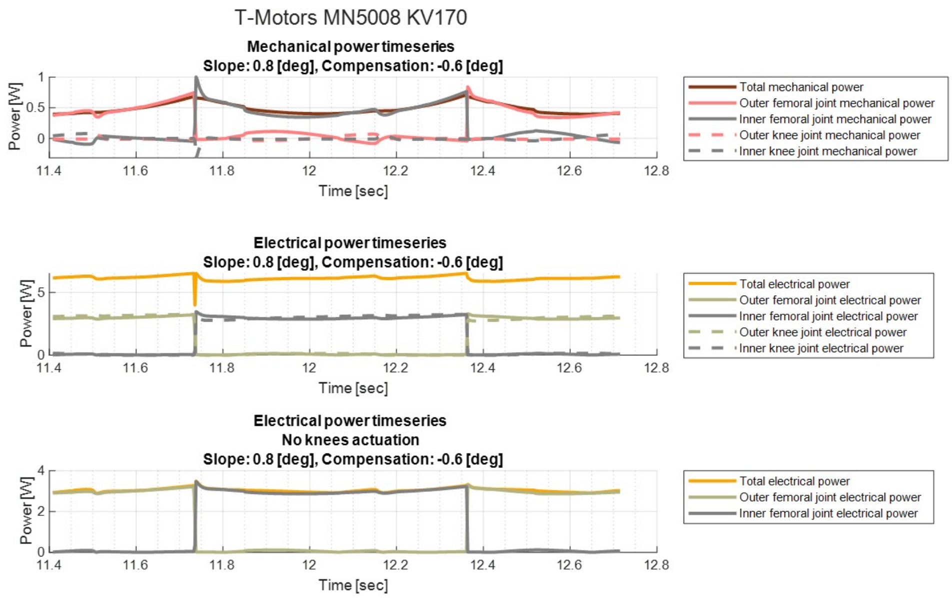

Figure 5.21: Mechanical power consumption, Electrical power consumption for full joint actuation, and electrical power consumption for no knees actuation.

5.5 Drivers

Because of the mechanical brushes absence, Brushless DC motors need electronic commutation to operate. Several drivers have been developed and are available for this reason. As the control scheme is torque control it is important to select a driver that can support torque/current control.

From previous experience in the CSL Lab T-Motor manufacturer does not provide detailed technical specifications for its motors. Additionally, the specifications provided are not considered accurate enough. It is noted that the motor characterization is not a straightforward process. Many brushless motor driver manufacturers considering this provide Motor identification routines integrated into the driver's firmware which can be very useful for accelerating the actuation system development procedure.

From the comparison of different drivers available is concluded that the best option for the specific application is the Tinymovr R5.2 which is a very compact, cost-effective solution able to automatically set the gain for the current control of the motor by its motor calibration firmware and additionally is manufactured in Greece. Otherwise, ODrive is a higher-cost solution that additionally supports cogging compensation operation and has been used in the past at the laboratory. So its performance has been evaluated.

	Drivers comparison						
Driver	moteus r4.11	ODRIVE S1	SOLO PICO	Tinymovr R5.2	Tinymovr R5.2	FE060-5-CM	VESC 6 EDU
Manufacturer	MJBOTS	ODrive	SOLO	Tinymovr	Tinymovr	AMC	TRAMPA
Region	USA	Deutchland	Italy	Greece	Greece	Hungary	England
Price	99.00 €	150.00 €	79.00 €	99.00 €	89.00 €	_	162.00 €
Size	46x53 [mm]	66x50 [mm]	68x57	40x36 [mm]	29x29 [mm]	38x25[mm]	44x56[mm]
Mass	14.2 [g]	35 [g]	28 [g]	10 [g]	8[g]	22.7	35[g]
Magnetic Enc.	Yes AS5047P-14bits Absolute	Yes MA702 Absolute	No	Yes	Yes	No	No
Voltage input	10-44 [V]	12-48 [V]	8-58[V]	12.0-38.0[V]	12.0-38.0[V]	12-48[V]	2-6S
Cont. ph.	11A/22A	20A	16[A]	40[A]	5 [A]	5[A]	25[A]
Peak el. power	500 [w]	_	300 [w]	300 + [w]	_	272[W]	_
Pwm switch.	abe 15-60 [kHz]	24 [kHz]	table 8-80[kHz]	_	_	20 [KHz]	_
Communications	CAN-FD	USB, UART, STEP/DIR, Analog Voltage,	USB, UART, CANopen, Analog, PWM	CAN, UART, SPI,AUX/Hall Sensor	CAN, UART, SPI	CANopen, STEP/DIR, Indexing,	USB,CAN,UAVCAN, COMM, PPM/PWM,
Aut. self-tuning and motor param.	Yes	Yes	Yes	Yes	Yes	No	No
Cogging compensation	No	Yes	No	No	No	No	No
Braking	Flux Braking	Brake Choper	_	Flux Braking	Flux Braking	_	_
Image							

Figure 5.22: Comparison of brushless motor drivers candidates.

5.6 Battery

The active knee-walker, an electrically actuated mobile robot, necessitates a reliable power source. Lithium-ion batteries, renowned for their high energy density, low self-discharge rates, and extended cycle life constitute a good option. Lithium Polymer batteries (Li-Po) are particularly suitable. Li-Po batteries, commonly used in drones and radio-controlled models, offer flexibility in customization for battery packs. With a nominal voltage of 3.7 volts, they can be easily connected in series to achieve the required voltages of $3.7 \times n$ [Volts]. These batteries are widely available in stores, contributing to their practicality for the project.

The selected battery must be compact to facilitate the spatial integration of electronics. Its capacity should support the uninterrupted execution of experimental procedures, and the discharge rate must be sufficient to power all electronic subsystems simultaneously. The alignment of battery specifications will be assessed after the motor selection procedure, as electrical power consumption demands can only be accurately calculated by considering the motor characteristics. The battery selected is the 'Tattu R-Line 550mAh 22.2V 6S1P 95C' (see Figure 5.23 due to its compact, size high discharge rate, and high voltage rating. The battery specifications are presented in the table 5.1.

Figure 5.23: Tattu R-Line 550mAh 22.2V 95C 6S1P Lipo Battery with XT30 has full capacity and discharge rate. It is a high discharge rate FPV racing lipo battery. The 95C gives you enough power under load. It is very compact in size and very light in weight

Spec.	Tattu R-Line 550mAh 22.2V
Capacity [mAh]	550
Num. Of Cells	6
Discharge Rate [h^{-1}]	95
Net Weight [g]	86
Dimensions [mm]	61×17×40

Table 5.1: Tattu R-Line 550mAh 22.2V specifications.

The maximum power consumption of the system is shown in Figure 5.21. The energy consumed by each complete step during the ascending of a 0.8^O slope ($E^{0.8^o}_{el.step}$) is calculated by integrating the total electric power ($P^{0.8^o}_{el.}$) to the time domain for this calculation it is assumed that the robot is fully actuated for safety (see Figure 5.7.

$$E^{0.8^o}_{el.step} = \int_{t=t_0}^{t=t_{end}} P^{0.8^o}_{el} \cdot dt \approx 8[Joule/step] \tag{5.7}$$

The total energy capacity of the battery is calculated as well as the total steps capability of the robot is calculated. in equation 5.9

$$E_{battery} = Capacity \cdot Voltage = 43957[Joule] \tag{5.8}$$

By dividing the total batteries capacity with the energy consumed by each complete step during the ascending of a 0.8^O slope, the total robot's steps capability is calculated (see equation **??**) which is considered far from enough. It is noted that the losses to the bearing are considered relatively small and have not been included in the calculation.

$$N_{steps} = \frac{E_{battery}}{E^{0.8^o}_{el.step}} \approx 5490[steps] \quad (5.9)$$

From the batteries discharge the current provision capabilities can be calculated. It emerges that the battery can provide effectively high powers $P_{battery,max}$ needed for the gait (see equation 5.10).

$$P_{battery,max} = Capacity \cdot Voltage \cdot Dis.Rate = 1160[Watt] \quad (5.10)$$